

THE SPATIAL CLUSTERING OF *ROSAT* ALL-SKY SURVEY AGNS
I. THE CROSS-CORRELATION FUNCTION WITH SDSS LUMINOUS RED GALAXIES

MIRKO KRUMPE¹, TAKAMITSU MIYAJI^{2,1}, AND ALISON L. COIL¹

Draft version October 30, 2018

ABSTRACT

We investigate the clustering properties of ~ 1550 broad-line active galactic nuclei (AGNs) at $\langle z \rangle = 0.25$ detected in the *ROSAT* All-Sky Survey (RASS) through their measured cross-correlation function with ~ 46000 Luminous Red Galaxies (LRGs) in the Sloan Digital Sky Survey. By measuring the cross-correlation of our AGN sample with a larger tracer set of LRGs, we both minimize shot noise errors due to the relatively small AGN sample size and avoid systematic errors due to the spatially-varying Galactic absorption that would affect direct measurements of the auto-correlation function (ACF) of the AGN sample. The measured ACF correlation length for the total RASS-AGN sample ($\langle L_X^{0.1-2.4 \text{ keV}} \rangle = 1.5 \times 10^{44} \text{ erg s}^{-1}$) is $r_0 = 4.3_{-0.5}^{+0.4} h^{-1} \text{ Mpc}$ and the slope $\gamma = 1.7_{-0.1}^{+0.1}$. Splitting the sample into low and high L_X samples at $L_X^{0.5-10 \text{ keV}} = 10^{44} \text{ erg s}^{-1}$, we detect an X-ray luminosity-dependence of the clustering amplitude at the $\sim 2.5\sigma$ level. The low L_X sample has $r_0 = 3.3_{-0.8}^{+0.6} h^{-1} \text{ Mpc}$ ($\gamma = 1.7_{-0.3}^{+0.4}$), which is similar to the correlation length of blue star-forming galaxies at low redshift. The high L_X sample has $r_0 = 5.4_{-1.0}^{+0.7} h^{-1} \text{ Mpc}$ ($\gamma = 1.9_{-0.2}^{+0.2}$), which is consistent with the clustering of red galaxies. From the observed clustering amplitude, we infer that the typical dark matter halo (DMH) mass harboring RASS-AGNs with broad optical emission lines is $\log(M_{\text{DMH}}/(h^{-1} M_\odot)) = 12.6_{-0.3}^{+0.2}$, $11.8_{-\infty}^{+0.6}$, $13.1_{-0.4}^{+0.2}$ for the total, low L_X , and high L_X RASS-AGN samples, respectively.

Subject headings: galaxies: active — large-scale structure of universe — X-rays: galaxies

1. INTRODUCTION

Galaxies and active galactic nuclei (AGNs) are not distributed randomly in the universe. The small primordial fluctuations in the matter density field present in the very early universe have progressively grown through gravitational collapse to create the complex network of clusters, groups, filaments, and voids seen in the distribution of structure today. Galaxies and AGNs, as well as groups and clusters of galaxies, are believed to populate the collapsed dark matter halos (DMHs). The clustering of galaxies and AGNs therefore reflects the spatial distribution of dark matter in the universe. This allows clustering measurements to be used to derive cosmological parameters (e.g., Peacock et al. 2001; Abazajian et al. 2005). However, these measurements also allow us to study the complex physics which governs the creation and evolution of galaxies and AGNs, as well as the co-evolution of galaxies and AGNs. The co-evolution scenario is motivated by the observed correlation between the mass of the central super-massive black hole (SMBH) and the stellar velocity dispersion in the bulge (Gebhardt et al. 2000; Ferrarese & Merritt 2000), lending strong evidence to an interaction or feedback mechanism between the SMBH and the host galaxy. The specific form of the feedback mechanism, as well as the details of the AGN triggering, accretion, and fueling mechanisms, remains unclear. Different cosmological simulations ad-

dress possible scenarios for the co-evolution of AGNs and their host galaxies (e.g., Kauffmann & Haehnelt 2000; Di Matteo et al. 2005; Cattaneo et al. 2006). Large volume, high-resolution simulations that include physical prescriptions for galaxy evolution and AGN feedback make predictions for the spatial clustering and large-scale environments of AGNs and galaxies (Springel et al. 2005; Colberg & Di Matteo 2008; Bonoli et al. 2009). Observed clustering measurements of AGNs can be used to test these theoretical models, put constraints on the feedback mechanisms, identify the properties of the AGN host galaxies, and understand the accretion processes onto SMBHs and their fueling mechanism.

X-ray surveys allow us to identify AGN activity without contamination from the emission of the host galaxy, i.e., therefore efficiently detecting even low luminosity AGNs. In the current era of deep and wide-area X-ray surveys with extensive spectroscopic follow-up, measurements of the three-dimensional (3D) clustering of AGN in various redshift ranges are emerging (Coil et al. 2009; Gilli et al. 2005; Yang et al. 2006). However, our knowledge of AGN clustering in the low redshift universe ($z \lesssim 0.4$) is still poor, except for optically selected type II AGNs (Wake et al. 2004; Li et al. 2006). This is due to the lack of observable comoving volume and the low number density of low- z AGNs. Exceptionally large survey areas with good sensitivity are needed to acquire a sufficiently large number of objects for clustering measurements.

To date, the *ROSAT* All-Sky Survey (RASS; Voges et al. 1999) is the most sensitive survey to have mapped the entire sky in X-rays. Surveys with modern higher-sensitivity X-ray observatories such as *XMM-Newton* and *Chandra* cover much smaller areas of the

¹ University of California, San Diego, Center for Astrophysics and Space Sciences, 9500 Gilman Drive, La Jolla, CA 92093-0424, USA

² IAUNAM-E (Instituto de Astronomía de la Universidad Nacional Autónoma de México, Ensenada), P.O. Box 439027, San Diego, CA 92143-9027, USA
Electronic address: mkrumpe@ucsd.edu

sky (area: $\sim 0.1\text{-}10\text{ deg}^2$). Therefore, the available co-moving volume from these deeper data sets is not sufficient to accurately measure AGN clustering at low redshifts ($z \lesssim 0.4$). Serendipitous surveys, such as extended ChAMP (Covey et al. 2008) and 2XMM (Watson et al. 2009), cover larger areas ($\sim 33\text{ deg}^2$ and $\sim 360\text{ deg}^2$, respectively). However, the large variations in sensitivity between different observations and the non-contiguous sky coverage make serendipitous surveys unsuitable for wide-area clustering measurements.

A few studies have attempted to measure the auto-correlation function (ACF) of RASS-based AGN samples. Two-dimensional (2D) angular correlation functions (Akylas et al. 2000) do not require redshift measurements for each AGN, but the projection heavily dilutes the clustering signal. Furthermore, the deprojection of the angular clustering to the 3D correlation function is subject to uncertainties in the redshift distribution, which can be substantial. Direct measurements of the 3D RASS-AGN ACF with spectroscopic redshift measurements have been made by Mullis et al. (2004) and Grazian et al. (2004) with a few hundred AGNs, respectively, providing clustering measurements that have large statistical uncertainties caused by the relatively small sample size.

Anderson et al. (2003, 2007) positionally cross-correlated RASS sources with spectroscopic data available from the Sloan Digital Sky Survey (SDSS). This dramatically increased the number of RASS-AGNs with spectroscopic redshift measurements, which we use here to provide significant improvements in the measurement of AGN clustering at low redshift. Furthermore, the availability of spectroscopic redshifts for large samples of SDSS galaxies in the same volume allows us to use an alternative approach to infer the clustering of AGN using calculations of the AGN–galaxy cross-correlation function (CCF). This approach uses much larger samples of AGN–galaxy pairs and hence significantly reduces the uncertainties in the spatial correlation function compared with direct measurements of the AGN ACF. Furthermore, the use of a CCF avoids the problem that we have to correct for the complex angular dependences of limiting sensitivity in the X-ray sample.

We therefore have initiated a program to investigate the clustering properties of low redshift ($z \sim 0.25$) RASS-AGNs through measurements of the CCF of these AGNs with SDSS Luminous Red Galaxies (LRGs). In this study, we chose LRGs as the corresponding galaxy sample because they have a significant overlap in redshift range with our X-ray sample (details are described later).

In this first paper of a series, we explain the data selection, as well as the calculation of the CCF and the inferred RASS-AGN ACF. We also investigate the X-ray luminosity dependence of the clustering properties and biases. In a follow-up paper (T. Miyaji et al., in preparation), we will focus on applying the halo occupation distribution (HOD) model to the calculated CCF between RASS-AGNs and LRGs.

The paper is organized as follows. In Section 2, we describe the construction and properties of the LRG and X-ray AGN samples in details. All essential steps to measure the CCF, compute the ACF via the CCF, and estimate errors are explained in Section 3. The re-

sults of the clustering measurements for the different X-ray AGN samples and their luminosity dependence are given in Section 4. We discuss these results in Section 5 in the context of other studies and conclude in Section 6. Throughout the paper, all distances, luminosities, and absolute magnitudes are measured in co-moving coordinates and given in units of $h^{-1}\text{ Mpc}$, where $h = H_0/100\text{ km s}^{-1}$, unless otherwise stated. We use a cosmology of $\Omega_M = 0.3$ and $\Omega_\Lambda = 0.7$ (Spergel et al. 2003). We use AB magnitudes throughout the paper. All uncertainties represent a 1σ (68.3%) confidence interval unless otherwise stated.

2. DATA

2.1. SDSS Luminous Red Galaxy Sample

The optical data analyzed in this study are drawn from the SDSS (York et al. 2000). We use data both from the main galaxy sample, which has a spectroscopic depth of $r = 17.7$ (Strauss et al. 2002), and the LRG sample, which has a spectroscopic depth of $r = 19.5$, significantly fainter than the main galaxy sample. The LRG sample was designed for studies of large-scale structure to higher redshift; it covers a larger volume than the main galaxy sample. Here we use the LRG sample as a large-scale structure tracer set to calculate the CCF with the RASS-AGN, as the LRG sample covers a similar redshift range as the RASS-AGNs.

The target selection and the properties of the LRG sample are described in detail in Eisenstein et al. (2001). Two different selection criteria ('cut I' and 'cut II') were introduced in identifying LRGs as at $z \gtrsim 0.4$ the typical 4000 \AA break in the spectral energy distribution (SED) of an early-type galaxy drops out of the g band and falls into the r band. Eisenstein et al. (2001) shows that up to $z \sim 0.38$ a volume-limited sample of LRGs with passively evolving luminosity and rest-frame colors is selected with a very high efficiency (95% for cut I and 90% for cut II). Eisenstein et al. (2001) advised that the LRG selection algorithm should not be used for objects $z < 0.15$.

2.1.1. Extraction of the SDSS Luminous Red Galaxy Sample

The LRG sample was obtained using the web-based SDSS Catalog Archive Server Jobs System³. The appropriate objects are selected through the prime target flag 'galaxy_red' (Eisenstein et al. 2001). In SDSS DR2, the model magnitude code was changed (Abazajian et al. 2004) to improve the star–galaxy separation. This also caused a slight change in the LRG sample definition. We make use of the updated LRG sample selection.

We extract 115,577 LRGs in the DR7 data release that have a spectroscopic redshift of $z > 0.15$, a galaxy spectral-type classification, and a redshift confidence level of $z_{\text{conf.}} > 0.95$. We discovered that 3% of objects flagged 'galaxy_red' (i.e., both cut selections) in DR7 do not fall within the LRG selection criteria (see Eisenstein et al. 2001). This does not happen in earlier data releases prior to DR7.

To calculate the RASS-AGN–LRG CCF, we wish to define an LRG sample that is both volume-limited and contains a high number density of LRGs to maximize

³ <http://casjobs.sdss.org/CasJobs/>

the number of possible AGN–LRG pairs. Table 1 of Zehavi et al. (2005a) defines three different volume-limited LRG samples, corresponding to different luminosity ranges, that they use to measure the LRG ACF. The first volume-limited LRG sample, with $-23.2 < M_g < -21.2$ and $0.16 < z < 0.36$, contains the highest number density of objects. Here we adopt the same LRG sample definition, as this sample is the best suited to our scientific goals. We select LRGs from DR7 that meet the criteria of this sample, and we refer to the subsequent data here as ‘LRG sample’. We further limited our survey area to DR4+ to match the X-ray sample (see Section 2.3). The properties of this sample are shown in Table 1.

The selected LRGs span a range in redshift. To construct a volume-limited sample, one must correct their time-evolving SED to account for the evolution of the stellar population and the redshifting. As described in the Appendix of Eisenstein et al. (2001), we use the extinction corrected r_{petro}^* magnitude to construct the k -corrected and passively evolved rest-frame g_{petro}^* magnitudes (non-star-forming model). Zehavi et al. (2005a) passively evolve their M_g to $z = 0.3$ instead of $z = 0$ (Eisenstein et al. 2001; we refer to this magnitude by using the notation $M_g^{z=0.3}$). The stellar population synthesis (SPS) code described in Conroy et al. (2009) is used to derive the purely passive evolution correction. LRGs are $\Delta M_g = -0.27$ brighter at $z = 0.3$ compared to $z = 0$. This value is similar to the one used in Zehavi et al. (2005a) who state that the evolution is about 1 mag per unit redshift.

We extensively tested that our LRG sample meet the LRG selection criteria of both Eisenstein et al. (2001) and Zehavi et al. (2005a). We only consider objects that are located in areas of the sky that have a spectroscopic completeness fraction in DR7 of $f_{\text{compl}} > 0.8$. The vast majority of the objects in our sample (99.9%) belong to the LRG ‘cut I’ criteria.

2.1.2. Accounting for the SDSS Fiber Collision

Blanton et al. (2003a) describe the algorithm used for positioning tiles in the plane of the sky and assigning spectroscopic fibers for observing objects in the SDSS. The resulting spectroscopic sample of SDSS is spatially biased in that fibers on the same tile cannot be placed closer than 55 arcsec. Spectroscopic redshifts are available for galaxy pairs closer than 55 arcsec only if the field is observed at least twice. As discussed in Zehavi et al. (2002, 2005a), not taking into account the effects of these fiber collisions would systematically underestimate measured correlation functions, even on large scales. Blanton et al. (2005a) provide publicly available collision-corrected SDSS catalogs suitable for robust large-scale structure studies. They assign a redshift to a galaxy which has no spectroscopic redshift by giving it the redshift of that galaxy in a galaxy group that is positionally the closest and has a spectroscopic redshift. However, these catalogs are generated only for the main galaxy sample, not the LRG sample.

To correct our LRG sample for fiber collisions, we therefore use the following approach. We select from the SDSS catalog Archive Server all LRG objects that passed the pure photometric-based cut I and cut II selection

criteria, with no spectroscopic restrictions applied. Photometrically selected LRGs that get a redshift assigned are only those which have a spectroscopic LRG within a separation of $d < 55''$. This corresponds to 2% (1004 objects) of the total LRG sample. Our redshift assignment is a two stage process. First, if the photometrically selected LRG is included in the primary spectroscopic LRG sample but its redshift was initially rejected due to a low confidence level of $z_{\text{conf.}} \leq 0.95$, the spectroscopic redshift is now accepted independent of its confidence level to correct for fiber collisions. This specific procedure assigns a redshift only to nine objects.

As a next step, we make use of the substantially improved DR7 photometric redshift code (Abazajian et al. 2009) compared to earlier SDSS data releases. If the difference between the spectroscopic redshift ($z_{\text{spec},j}$) of an LRG and the photometric redshift ($z_{\text{photo},i}$) of a neighboring (within a 55 arcsecond radius) LRG is

$$|z_{\text{spec},j} - z_{\text{photo},i}| \leq \delta z_{\text{photo},i,1\sigma}, \quad (1)$$

then the photometric LRG is assigned the same redshift as the spectroscopic LRG. Otherwise the photometric redshift is taken to be the correct redshift for the photometric LRG. More than half of all photometric LRG redshifts are assigned the spectroscopic redshift of a neighboring LRG, while the remaining objects are assigned their photometric redshift.

The above procedure for redshift assignment is used because simply adopting the photometric redshift for all objects that do not have a measured spectroscopic redshift would smear out the clustering signal in redshift space and therefore dilute the amplitude of the correlation function. Blanton et al. (2003a) verified that for areas of the sky with overlapping spectroscopic tiles, 60% of the galaxies that had a neighboring galaxy within 55 arcsec were within 10 Mpc of the neighbor galaxy. Zehavi et al. (2005a) demonstrated that LRGs are highly clustered, so using this procedure for LRGs will result in a higher success rate. The average photometric redshift error ($\delta z/(1+z)$) is 2%, and within our sample less than 1% (437 objects) of the LRGs are assigned a photometric redshift.

2.2. The X-ray Sample

The RASS (Voges et al. 1999) is currently the most sensitive all-sky survey in the X-ray regime, with a typical flux limit of $f_X \sim 10^{-13} \text{ erg cm}^{-2} \text{ s}^{-1}$ (0.1–2.4 keV). The area of the sky covered is 99.7%, all of which has at least 50 s of exposure with *ROSAT* Position Sensitive Proportional Counters (PSPC).

Based on the SDSS data release 5 (DR5), Anderson et al. (2007) classify 6224 AGNs with broad permitted emission lines in excess of 1000 km s^{-1} FWHM and 515 narrow permitted emission line AGNs matching RASS sources within 1 arcmin (note that 86% of all matches fall within $30''$). Consequently, broad-line AGNs account for 92% of all RASS/SDSS classifications. In this study, we use the broad emission line RASS-AGNs only. The RASS sources are taken from both the RASS Bright source catalog (Voges et al. 1999) and the RASS Faint source catalog (Voges et al. 2000) and have a maximum likelihood $\text{ML} \geq 7$.⁴

⁴ Anderson et al. (2003, 2007) say that sources with $\text{ML} \geq 10$

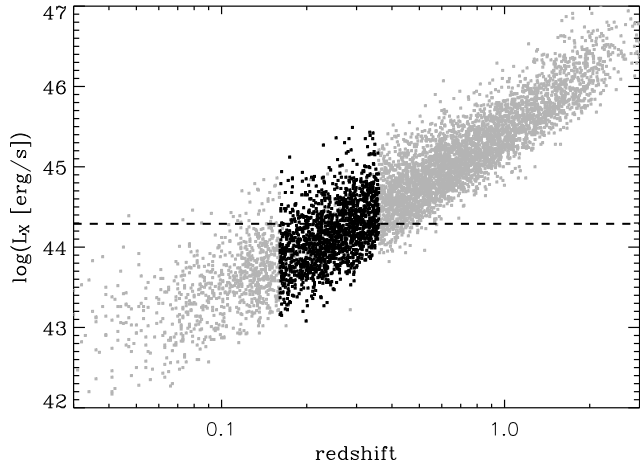


FIG. 1.— 0.1-2.4 keV X-ray luminosity vs. redshift for the broad emission line AGN sample in SDSS DR5 determined by Anderson et al. (2007). Black symbols show objects in the redshift range $0.16 < z < 0.36$, which define the AGN sample used here. The dashed line corresponds to the common dividing line between low luminous AGNs and high luminous QSOs ($L_X^{0.5-10 \text{ keV}} = 10^{44} \text{ erg s}^{-1}$) defining the low and high luminosity RASS-AGN samples used here.

The data cover an area of 5740 deg^2 . The derived luminosities in Anderson et al. (2007) are based on a flat Λ CDM cosmology with $(\Omega_M, \Omega_\Lambda, H_0) = (0.3, 0.7, 70 \text{ km s}^{-1} \text{ Mpc}^{-1})$.

The RASS/SDSS target selection consists of two selection algorithm: the main SDSS algorithm for galaxies and AGNs ($15.0 < m < 19.0$) and the specific assignment of SDSS fibers for RASS identifications ($15.0 < m < 20.5$). Anderson et al. (2003) explain in detail their selection of optical counterpart candidates.

To understand possible bias effects, which may influence our CCF measurements, we summarize the selection method briefly. The algorithm considers those SDSS optical objects within 1 arcmin of the X-ray source position. Optically detected objects qualify for SDSS spectroscopy if their g , r , or i magnitude is $15.0 < m < 20.5$. Since not every optically detected object that fulfills the criteria can be observed spectroscopically, different priority levels are introduced in target selection. The highest priority is given to objects with a triple positional coincidence of RASS X-ray source, SDSS optical object, and FIRST (Becker, White, & Helfand 1995) radio source. The next priority level consists of SDSS objects in the RASS error circles with unusual optical colors indicating AGNs (e.g., UV-excess with $u - g < 0.6$). The third priority includes less likely, but plausible, counterparts such as bright stars and galaxies. The last group consists of any object in the magnitude limit that falls within the RASS error circle. One RASS/SDSS spectroscopic fiber is assigned to the object with the highest priority level and a spatial offset less than 27.5 arcsec from the X-ray source. If multiple objects populate the same priority level, one is chosen at random for SDSS spectroscopy.

Before consideration is given to potential RASS targets, an SDSS fiber is first assigned to objects that belong

have been included. However, investigating the sample shows that $ML \geq 7$ has been used.

to the main SDSS sample, which includes both galaxies and optically identified AGNs. About 80% of all RASS/SDSS identifications are independently targeted for spectroscopy by the SDSS main target selection algorithm. However, objects in the main sample can be observed at the cost of excluding high-priority RASS targets. In these cases, the RASS/SDSS identification is missing. For these reasons, the RASS/SDSS AGN sample is only reasonably complete ($\gtrsim 90\%$) for AGNs with $15.0 < m < 19.0$.

Objects identified by RASS/SDSS priority levels and not because of their belonging to the main SDSS sample tend to be optically fainter, on average, than the main AGN sample. In the $u - g$ versus $g - r$ color-color space, objects from both selection algorithms lie in the same region. Studying their redshift distributions shows that objects identified by the RASS/SDSS priority levels are, on average, at higher redshifts than the identifications relying on the main SDSS sample. This also explains their lower observed count rates X-ray fluxes. The X-ray hardness ratios of both populations are very similar. Being fainter in X-rays and in the optical wavelengths leads to the same X-ray to optical flux ratio for the RASS/SDSS priority levels AGNs and the main SDSS sample AGNs. Therefore, except that RASS/SDSS priority levels AGNs are found on average at higher redshifts, no intrinsic differences between the RASS/SDSS AGNs from both selection methods are detected.

To create a well-defined X-ray AGN sample to use for clustering measurements, we focus solely on broad emission line AGNs. *ROSAT*'s sensitivity to the soft energy band that is limited to $< 2.4 \text{ keV}$ selects against X-ray absorbed AGNs (type II), which are usually optically classified as narrow line objects. Therefore, the sample of broad emission line RASS-AGN is much more complete than the narrow emission line RASS-AGN sample. Furthermore, the X-ray/optical counterpart identification is more reliable for the broad emission line AGNs than for the narrow emission line AGNs, which have much higher surface density (see Anderson et al. 2003, 2007 for details).

In addition to studying the clustering of the RASS-AGN sample, here we also test for possible differences in the clustering of low versus high X-ray luminosity RASS-AGN (Figure 1). The commonly used X-ray dividing line between Seyfert AGNs and high luminous QSOs is $L_X^{0.5-10 \text{ keV}} = 10^{44} \text{ erg s}^{-1}$ in the 0.5-10 keV band (intrinsic luminosity; Mainieri et al. 2002). Although this dividing line is somewhat arbitrary, it is widely employed in literature, and we use it here. Anderson et al. (2007) provide a table which list the galactic absorption-corrected 0.1-2.4 keV luminosities assuming a photon index of $\Gamma = 2.5$. With this index, the AGN/QSO dividing line corresponds to a 0.1-2.4 keV luminosity of $\log(L_X / (\text{erg s}^{-1})) = 44.298$ (Figure 1). This index agrees well with that found by Piconcelli et al. (2005) in the *XMM-Newton* spectra of PG quasars in the 0.5-2 keV band, where $\bar{\Gamma} = 2.73_{-0.11}^{+0.12}$. In the same paper, it is shown that at higher energies (2-12 keV) the mean photon index for PG quasars gets harder and is $\bar{\Gamma} = 1.89 \pm 0.11$. Here we use $\Gamma = 2.5$ to be consistent with Anderson et al. (2007).

The properties of our total RASS-AGN sample, low L_X

RASS-AGN sample, and the high L_X RASS-AGN sample are shown in Table 1. In order to measure the CCF of the RASS X-ray AGNs with LRGs, the X-ray samples must cover the same area of sky and redshift range as the LRG sample used here. In all samples, no X-ray detected AGN is also classified as an LRG. However, we cannot exclude the possibility that RASS-AGNs are hosted by LRGs and outshine their host galaxies. In contrast to the high L_X RASS-AGN sample, the total RASS-AGN sample and the low L_X RASS-AGN sample are not volume-limited. We calculate the comoving number density in Table 1 of these two samples in the following way. For a specific R.A. and decl. (contained in the DR4+ geometry), we determine the galactic absorption value N_H and the RASS exposure time. The RASS faint source catalog contains sources with at least six source counts. The latter leads to a limiting observable count rate for a given R.A. and decl. Using `Xspec`, we can compute the Galactic absorption-corrected flux limit versus survey area for the RASS-AGN based on count rates, N_H values, and $\Gamma = 2.5$. We then compute the comoving volume ($z_{\text{low}} = 0.16$) available to each object (V_a) for being included in the sample following Avni & Bahcall (1980), using the Galactic absorption-corrected object fluxes from Anderson et al. (2007). From this we calculate the comoving number density as $n_{\text{AGN}} = \sum_i 1/V_{a,i}$, where i sums over each object.

2.3. Defining a Common Survey Geometry of the RASS-AGN and LRG Samples

The RASS/SDSS Anderson et al. (2007) sample is based on the SDSS DR5, while the LRG sample is drawn from SDSS DR7. We make use of DR7 for the LRG sample as it contains the latest available and furthest advanced version of the SDSS products. Numerous correction have been applied in comparison to earlier data releases (see Abazajian et al. 2009; e.g., updated photo- z , repeated observations for few regions with poor seeing in previous data releases, filling holes in DR6 region, correction of instability in the spectroscopic flat-fields). We then limit our LRG sample to the region covered by the Anderson et al. (2007) AGN sample for the CCF calculation.

The SDSS survey geometry and completeness are expressed in terms of spherical polygons (Hamilton & Tegmark 2004). Publicly available geometry and completeness files are not available for DR5, which would have the largest common survey area between the LRG and the RASS-AGN samples. Therefore, we use the latest version available prior to DR5: the DR4+ geometry file,⁵ which is a subset (Park et al. 2007) of the SDSS DR5 (Adelman-McCarthy et al. 2007) and covers 5540 deg² (DR5: 5740 deg²).

The final, fiber collision-corrected LRG sample used here is based on DR7 but reconfigured to include only the DR4+ survey area that has DR7 completeness ratios of $f_{\text{compl}} > 0.8$. The corresponding area of the total sample is 5468 deg². This reconfiguration of the total Anderson et al. (2007) sample from DR5 to DR4+ eliminates 287 broad emission line objects, leaving 5937 AGNs. Applying the redshift range selection of the LRG sample results in the number of objects given in Table 1

for each AGN sample. Figure 2 shows the sky coverage of our final RASS-AGN sample and the LRG sample re-configured to a common DR4+ geometry which is used for the calculation of the CCF.

3. MEASURING THE CROSS-CORRELATION FUNCTION

A commonly used technique for measuring the spatial clustering of a class of objects is the two-point correlation function $\xi(r)$ (Peebles 1980), which measures the excess probability dP above a Poisson distribution of finding an object in a volume element dV at a distance r from another randomly chosen object:

$$dP = n[1 + \xi(r)]dV, \quad (2)$$

where n is the mean number density of objects. The ACF measures the excess probability of finding two objects from the same sample in a given volume element, while the CCF measures the excess probability finding an object from one sample at a distance r from another object drawn from a different sample. The two-point correlation function, $\xi(r)$, is equal to 0 for randomly distributed objects, and $\xi(r) > 0$ if objects are more strongly clustered than a randomly distributed sample.

In practice, the correlation function is obtained by counting pairs of objects with a given separation and comparing to the number of pairs in a random sample for the same separation. Different correlation estimators are described in the literature. Davis & Peebles (1983) give a simple estimator with the form

$$\xi(r) = \frac{DD(r)}{DR(r)} - 1, \quad (3)$$

where $DD(r)$ is the sum of the data–data pairs at the separation r and $DR(r)$ is the number data–random pairs; both pair counts have been normalized. Landy & Szalay (1993) suggest a more advanced estimator:

$$\xi = \frac{1}{RR} [DD - 2DR + RR], \quad (4)$$

where RR is the normalized number of random–random pairs; this estimator yields errors similar to what is expected for Poisson errors only.

Because we measure line-of-sight distances from redshifts, the measurement of ξ is subject to the redshift-space distortions due to peculiar velocities. To separate the effects of redshift distortions, the spatial correlation function is measured as a function of two components of the separation vector between two objects, i.e., one perpendicular to (r_p) and the other along (π) the line of sight. Therefore, $\xi(r_p, \pi)$ is extracted by counting pairs on a 2D grid of separations r_p and π . The real-space correlation function $\xi(r)$ can be recovered by integrating along the π direction and computing the projected correlation function by Davis & Peebles (1983)

$$\begin{aligned} w_p(r_p) &= 2 \int_0^\infty d\pi \xi(r_p, \pi) \\ &= 2 \int_0^\infty dy \xi \left[(r_p^2 + y^2)^{1/2} \right] \\ &= 2 \int_{r_p}^\infty r dr \xi(r) (r^2 - r_p^2)^{-1/2} \end{aligned} \quad (5)$$

which is independent of redshift-space distortions. The variable y represents the real-space separation along the

⁵ <http://sdss.physics.nyu.edu/lss/dr4plus>

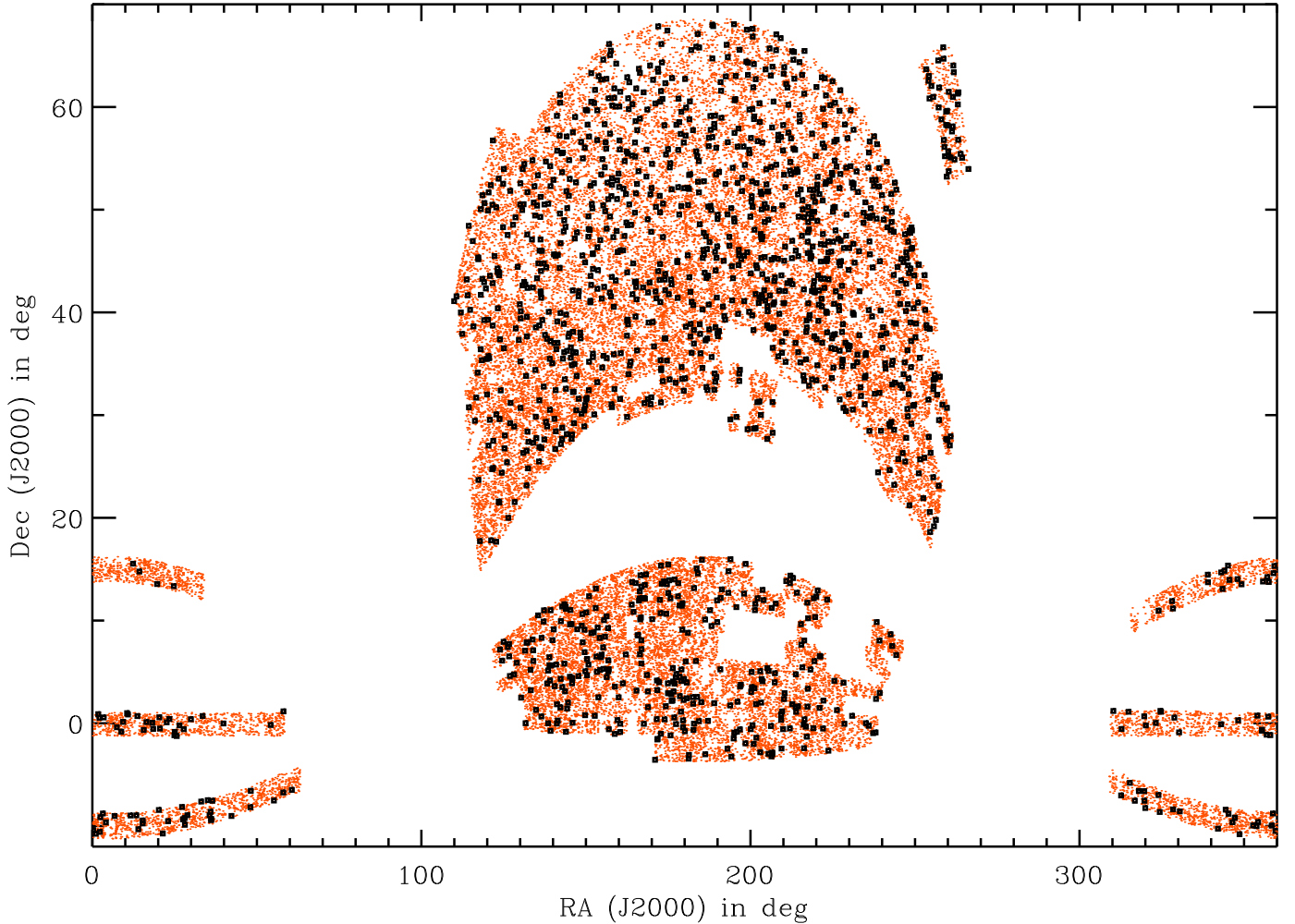


FIG. 2.— Spatial distribution of the total RASS-AGN sample (black squares) and SDSS LRG sample used here (dots, our LRG sample) restricted to the SDSS DR4+ geometry. The total covered area is 5468 deg².

TABLE 1. PROPERTIES OF THE LRG AND RASS-AGN SAMPLES.

Sample Name	z -range	$M_g^{z=0.3}$ Range (mag)	Number	$\langle n_{\text{LRG}} \rangle$ ($h^3 \text{ Mpc}^{-3}$)	$\langle z \rangle$	$\langle M_g^{z=0.3} \rangle$ (mag)
LRG sample	$0.16 < z < 0.36$	$-23.2 < M_g^{z=0.3} < -21.2$	45899	9.6×10^{-5}	0.28	-21.71
	z -range	$L_X^{0.1-2.4 \text{ keV}}$ Range (erg s ⁻¹)	Number	$\langle n_{\text{AGN}} \rangle$ ($h^3 \text{ Mpc}^{-3}$)	$\langle z \rangle$	$\langle L_X^{0.1-2.4 \text{ keV}} \rangle$ (erg s ⁻¹)
Total RASS-AGN sample	$0.16 < z < 0.36$	—	1552	6.0×10^{-5}	0.25	1.49×10^{44}
Low L_X RASS-AGN sample	$0.16 < z < 0.36$	$L_X \leq 1.95 \times 10^{44}$	990	5.8×10^{-5}	0.24	8.81×10^{43}
High L_X RASS-AGN sample	$0.16 < z < 0.36$	$L_X > 1.95 \times 10^{44}$	562	1.2×10^{-6}	0.28	3.78×10^{44}

line of sight. For a power law correlation function

$$\xi(r) = \left(\frac{r}{r_0} \right)^{-\gamma}, \quad (6)$$

r_0 and γ are readily extracted from the projected correlation function using the analytical solution

$$w_p(r_p) = r_p \left(\frac{r_0}{r_p} \right)^\gamma \frac{\Gamma(1/2)\Gamma((\gamma-1)/2)}{\Gamma(\gamma/2)}, \quad (7)$$

where $\Gamma(x)$ is the Gamma function.

The aim of this paper is to more accurately measure the clustering properties of low- z AGNs than has

been measured previously using ACFs (e.g., Mullis et al. 2004; Grazian et al. 2004); we accomplish this by measuring the CCF of the AGNs with higher-density LRGs in the same volume. Assuming a linear bias, we follow Coil et al. (2009) and infer the ACF of the AGN sample using

$$w_p(\text{AGN}|\text{AGN}) = \frac{[w_p(\text{AGN}|\text{LRG})]^2}{w_p(\text{LRG}|\text{LRG})}, \quad (8)$$

where $w_p(\text{AGN}|\text{AGN})$ and $w_p(\text{LRG}|\text{LRG})$ are the ACFs of the RASS-AGNs and the LRGs, respectively, and $w_p(\text{AGN}|\text{LRG})$ is the CCF of the RASS-AGNs with

the LRGs. The LRG ACF is studied extensively in Zehavi et al. (2005a), where the estimator in Equation (4) is used; the results are given here in Table 2. The RASS-AGN–LRG CCF is computed here using the estimator given in Equation (3)

$$\xi_{\text{AGN-LRG}} = \frac{D_{\text{AGN}} D_{\text{LRG}}}{D_{\text{AGN}} R_{\text{LRG}}} - 1. \quad (9)$$

We use this estimator as it requires a random catalog for only the LRG sample (R_{LRG}), which is homogeneous, volume-limited, and has a well-understood selection function. The estimator given in Equation (4) would require a random catalog for the RASS-AGN sample, which would be subject to possible systematic biases due to difficulties in accurately modeling the position-dependent sensitivity limit. Especially, the changing Galactic absorption over the sky causes variations in the flux limit, which would require spectrum-dependent corrections.

3.1. Construction of the Random LRG Sample

The generation of random samples is crucial for a proper measurements of the correlation function. The objective is to construct a sample of randomly distributed sources that have the same observational survey biases as the real sample. Use of the estimator given in Equation (3) requires that the construction of a random sample for only the LRG population is needed.

The LRG sample used here has been corrected for fiber collisions (Section 2.1.2); therefore, we do not have to consider this bias in the construction of the random LRG sample. The SDSS survey geometry and completeness ratio for a given field are given by the SDSS geometry files. For a set of random R.A. and decl. values, they allow us to determine if an object is covered by the SDSS DR4+ geometry and the spectroscopic completeness ratio at that location. Only objects covered in DR4+ with a DR7 spectroscopic completeness ratio $f_{\text{compl}} > 0.8$ are accepted for the random sample required here. Additionally, the DR7 spectroscopic completeness is used as the probability that an object is kept for the random sample. If the completeness ratio is 0.9, the object has a 90% chance of being included in the final random LRG sample. This procedure takes into account the fact that survey regions with a high spectroscopic completeness ratio have, on average, a higher object density than less complete areas.

The corresponding redshift for a random object is assigned based on the smoothed redshift distribution of the LRG data sample. The smoothing has been made by applying a least-squares (Savitzky & Golay 1964) low-pass filter to the observed LRG redshift distribution. We compare the redshift distribution of the LRG data sample, its smoothed profile, and the redshift distribution of the random LRG sample in Figure 3. The shape of the LRG redshift distribution is caused by the superposition of two selection criteria for the LRGs. At low redshifts, most of the LRGs are selected in the SDSS main galaxy sample. This flux-limited selection reaches the maximum at $z \sim 0.22$. The 'cut I' LRG selection provides objects already from the lowest redshifts with a fast increasing number of objects for higher redshifts. This selection reaches its flux limit at $z \sim 0.35$. The 'cut II' selection plays an important role only at $z \gtrsim 0.42$. The selection

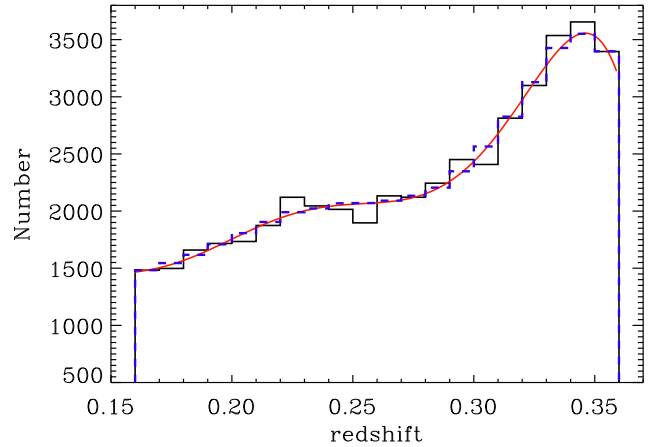


FIG. 3.— Redshift histogram of the LRG data sample (solid black lines), the smoothed profile (red), and the random LRG sample (blue-dashed, renormalized to the total number of LRGs).

dependence in different redshifts is illustrated in detail in Figure 12–14 of Eisenstein et al. (2001).

The random catalog contains 100 times as many objects as the LRG sample. This value is chosen to have an adequate number of pairs in the $D_{\text{AGN}} R_{\text{LRG}}$ sample at the smallest scales measured here.

3.2. Errors and Covariance Matrices

The calculation of realistic error bars on measurements of the correlation function has been a subject of debate since the earliest measurements. Different methods are summarized in Norberg et al. (2009). Adjacent bins in $w_p(r_p)$ are correlated, as are their errors. The construction of a covariance matrix M_{ij} , which reflects the degree to which bin i is correlated with bin j , is needed to obtain meaningful power law fits to $w_p(r_p)$.

We estimate the statistical errors of our correlation measurements using the jackknife method. We divide the survey area into $N_T = 100$ sections, each of which is ~ 55 deg². We calculate $w_p(r_p)$ N_T times, where each jackknife sample excludes one section. These N_T jackknife-resampled RASS-AGN ACFs are used to derive the covariance matrix M_{ij} by

$$M_{ij} = \frac{N_T - 1}{N_T} \left[\sum_{k=1}^{N_T} \left(w_k(r_{p,i}) - \langle w(r_{p,i}) \rangle \right) \times \left(w_k(r_{p,j}) - \langle w(r_{p,j}) \rangle \right) \right] \quad (10)$$

where $w_k(r_{p,i})$ and $w_k(r_{p,j})$ are from the k -th jackknife samples of the RASS-AGN ACF and $\langle w(r_{p,i}) \rangle$, $\langle w(r_{p,j}) \rangle$ are the averages over all of the jackknife samples. The 1σ error of each bin is the square root of the diagonal component of this matrix ($\sigma_i = \sqrt{M_{ii}}$). To calculate the covariance matrix of the RASS-AGN ACF, which is determined using Equation (8), we compute the RASS-AGN ACF for each of the N_T jackknife samples from the corresponding RASS-AGN–LRG CCF and LRG ACF of each jackknife sample.

3.3. The RASS-AGN Auto-correlation Function

TABLE 2. RESULTS OF POWER LAW FITS TO THE LRG ACFs AND RASS-AGN-LRG CCFs

Sample	r_0 (h^{-1} Mpc)	γ
Our LRG sample	$9.68^{+0.14}_{-0.14}$	$1.96^{+0.02}_{-0.02}$
Zehavi subsample1	9.80 ± 0.20	1.94 ± 0.02
Total RASS-AGN sample	$6.93^{+0.27}_{-0.28}$	$1.86^{+0.04}_{-0.04}$
Low L_X RASS-AGN sample	$6.12^{+0.50}_{-0.53}$	$1.94^{+0.10}_{-0.08}$
High L_X RASS-AGN sample	$7.74^{+0.40}_{-0.43}$	$1.92^{+0.08}_{-0.08}$

NOTE. — Values of r_0 and γ are obtained from a power law fit to $w_p(r_p)$ over the range $r_p=0.3-40 h^{-1}$ Mpc for all samples using the full error covariance matrix. For the LRG ACFs, Zehavi et al. (2005a) and we used a $\pi_{\max} = 80 h^{-1}$ Mpc, while for all CCFs $\pi_{\max} = 40 h^{-1}$ Mpc was applied.

We compute the CCF between RASS-AGNs and LRGs for the total sample, the low L_X sample, and the high L_X sample (see Table 2), as well as the ACF of the LRGs. We measure r_p in a range of $0.3-40 h^{-1}$ Mpc in 11 bins in a logarithmic scale, while π is computed in steps of $5 h^{-1}$ Mpc in a range of $\pi = 0 - 200 h^{-1}$ Mpc. The resulting $\xi(r_p, \pi)$ are shown in Figure 4 for $r_p = 0 - 30 h^{-1}$ Mpc and $\pi = 0 - 80 h^{-1}$ Mpc. Note the flattened contour at $\pi \sim 40 h^{-1}$ Mpc in the LRG ACF. This is the first direct observation of the coherent infall for LRGs as expected by the Kaiser effect (Kaiser 1987).

Although Equation (5) requires an integration over π to infinity, in practice an upper bound of integration (π_{\max}) is used:

$$w_p(r_p) = 2 \int_0^{\pi_{\max}} d\pi \xi(r_p, \pi). \quad (11)$$

The value of π_{\max} has to be large enough to include most correlated pairs and give a stable solution, but not be so large as to unnecessarily increase the noise in the measurement. To determine the appropriated π_{\max} values for our correlation functions, we determined the correlation length r_0 for a set of π_{\max} values by fitting $w_p(r_p)$ with a fixed $\gamma = 1.9$ over a r_p range of $0.3-40 h^{-1}$ Mpc.

Figure 5 shows that the LRG ACF saturates at $\pi_{\max} = 80 h^{-1}$ Mpc. The changes in the correlation lengths above this value are well within the uncertainties. Therefore, as in Zehavi et al. (2005a), we use an upper bound of the LRG ACF integration of $\pi_{\max} = 80 h^{-1}$ Mpc. Table 2 shows the values of r_0 and γ for a power law fit in a range of $0.3-40 h^{-1}$ Mpc (as used in Zehavi et al. 2005a). Both results well agree within their uncertainties.

The CCFs between the different RASS-AGN samples and the LRGs saturate at $\pi_{\max} = 40 h^{-1}$ Mpc (Figure 5). At higher values of π_{\max} , the signal-to-noise ratio degrades and no significant change in r_0 occurs. Therefore, we use $\pi_{\max} = 40 h^{-1}$ Mpc as an upper bound of integration for all AGN-LRG CCFs. The difference in the measured LRG ACF using $\pi_{\max} = 40 h^{-1}$ Mpc and $\pi_{\max} = 80 h^{-1}$ Mpc is only 3%. We expect that the growth of the CCF between $\pi_{\max} = 40 h^{-1}$ Mpc and $\pi_{\max} = 80 h^{-1}$ Mpc is about the same order. Since this is much smaller than the errors in the CCF, a use of $\pi_{\max} = 40 h^{-1}$ Mpc for the CCF is reasonable. The correlation length of the CCFs of the different RASS-AGN

samples and the LRGs is given in Table 2.

As the area covered by SDSS DR4+ is not contiguous (see Figure 2), we computed the CCF for different subsamples of the SDSS DR4+, to check that there were no biases introduced by using non-contiguous regions of the sky. Excluding survey areas with R.A. $< 70^\circ$ and R.A. $> 300^\circ$, the isolated area around R.A. $\sim 260^\circ$ and decl. $\sim 60^\circ$, the somewhat patchy areas at $190^\circ < \text{R.A.} < 250^\circ$ and $0^\circ < \text{decl.} < 35^\circ$, and combinations thereof, results in measurements of the CCFs that all agree well within their uncertainties. Changing the step size of π from 5 to $2.5 h^{-1}$ Mpc alters $w_p(r_p)$ by a negligible amount.

Instead of using the derived values of r_0 from the power law fits of the LRG ACF and AGN-LRG CCFs to compute the RASS-AGN ACF, we use Equation (8) and use the full $w_p(r_p)$ functions. Figure 6 shows $w_p(r_p)$ for the RASS-AGN ACF, the LRG ACF, and the RASS-AGN-LRG CCF. Figure 7 shows the CCFs for the low and high L_X RASS-AGN samples.

We fit power laws to the ACFs of the different RASS-AGN samples. The fit uses the covariance matrix and minimizes the correlated χ^2 values according to

$$\chi^2 = \sum_{i=1}^{N_{\text{bins}}} \sum_{j=1}^{N_{\text{bins}}} \left(w_p(r_{p,i}) - w_p^{\text{model}}(r_{p,i}) \right) \times M_{ij}^{-1} \left(w_p(r_{p,j}) - w_p^{\text{model}}(r_{p,j}) \right) \quad (12)$$

We only fit the data in a range $r_p = 0.3-15 h^{-1}$ Mpc, as the clustering signal above $r_p = 15 h^{-1}$ Mpc is not well-constrained for the low L_X RASS-AGN sample. The upper end of r_p has also been chosen because we will later convert the fit results into $\sigma_{8,\text{AGN}}$ which involves only the pairs within $16 h^{-1}$ Mpc. Contour plots of the resulting values of r_0 and γ are shown in Figure 8 for the different RASS-AGN samples. The derived best-fit values, as well as the best-fit r_0 values with a fixed power law slope of $\gamma = 1.9$, are given in Table 3. Based on the error on r_0 for a fixed $\gamma = 1.9$, we estimate the clustering signal to be detected at a $\sim 11\sigma$, $\sim 5\sigma$, and $\sim 8\sigma$ level for the total, the low L_X , and the high L_X RASS-AGN sample, respectively. The difference in the clustering signal between the low L_X , and the high L_X RASS-AGN sample is detected at the $\sim 2.5\sigma$ level.

The clustering strength is commonly expressed in terms of the rms fluctuation of the density distribution over the sphere with a comoving radius of $8 h^{-1}$ Mpc. For a power law correlation function, this value can be calculated by (Miyaji et al. 2007; Section 59 of Peebles 1980)

$$(\sigma_{8,\text{AGN}})^2 = J_2(\gamma) \left(\frac{r_0}{8 h^{-1} \text{Mpc}} \right)^\gamma, \quad (13)$$

where $J_2(\gamma) = 72 / [(3 - \gamma)(4 - \gamma)(6 - \gamma)2^\gamma]$. The uncertainty of $\sigma_{8,\text{AGN}}$ is computed from the r_0 versus γ confidence contour of the one-parameter fit based on a correlated $\chi^2 = \chi_{\text{min}}^2 + 1.0$ (Figure 8).

Based on $\sigma_{8,\text{AGN}}$, we further calculate the RASS-AGN bias parameter $b = \sigma_{8,\text{AGN}}(z) / \sigma_8(z)$. This quantity allows us to compare the observed AGN clustering to the underlying mass distribution from linear growth theory (Hamilton 2001). We use a normalization to a value of

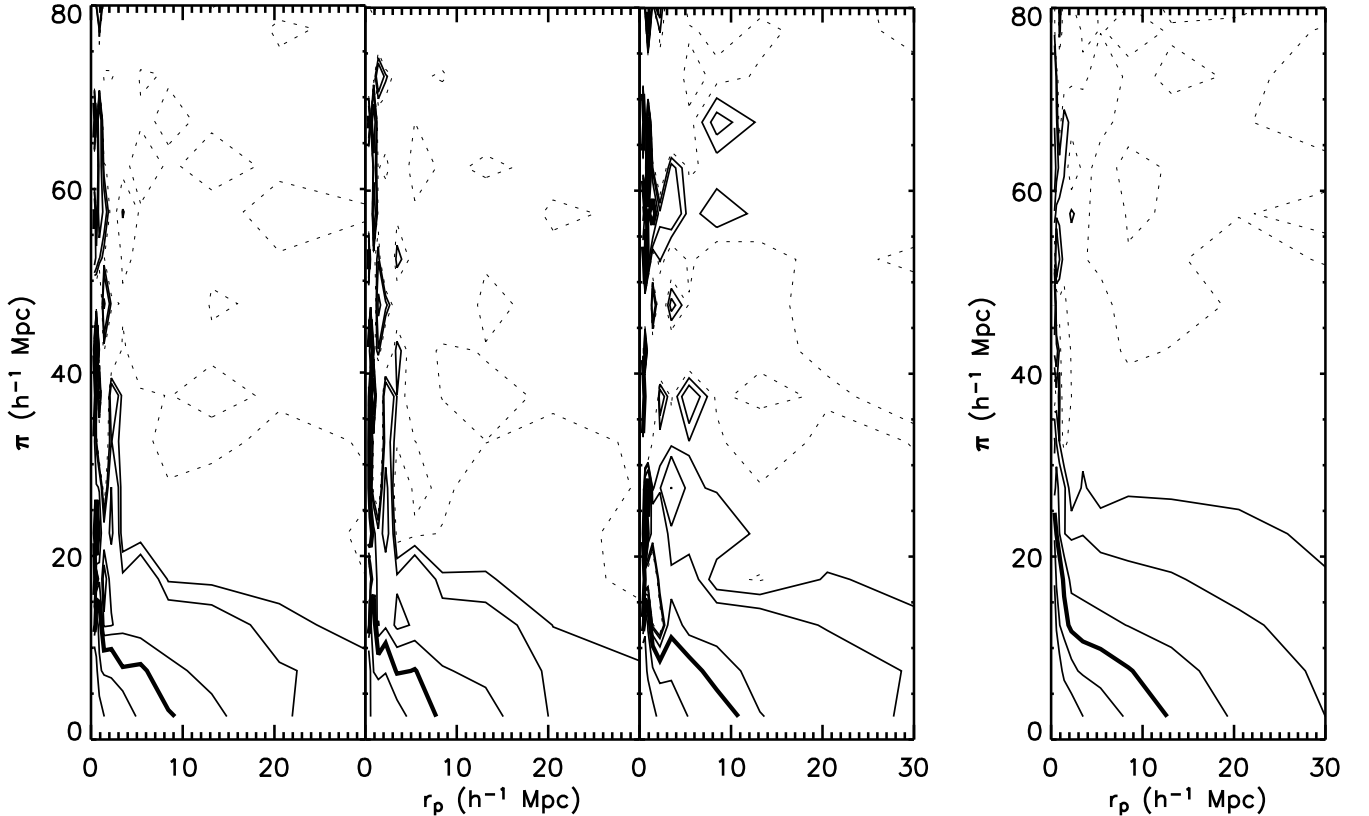


FIG. 4.— Contour plot of the CCF between RASS-AGNs and LRGs for the total sample, the low L_X AGN sample, the high L_X AGN sample, as well as the LRG ACF (left to right). Contour lines show constant correlation strength for the 2D correlation function $\xi(r_P, \pi)$. The data are not smoothed. The contour levels are 0.0 (dotted line), 0.1, 0.2, 0.5, 1.0 (thick solid line), 2.0, and 5.0.

TABLE 3. POWER LAW FITS TO THE RASS-AGN ACF.

Sample Name	r_0 (h^{-1} Mpc)	γ	$r_{c, \gamma=1.9}$ (h^{-1} Mpc)	$\sigma_{8, \text{AGN}}(z)$	$b(z)$ ($\sigma_{8, \text{AGN}}(z)/\sigma_8(z)$)	$\log M_{\text{DMH}}$ ($h^{-1} M_\odot$)
Total RASS-AGN sample	$4.28^{+0.44}_{-0.54}$	$1.67^{+0.13}_{-0.12}$	$4.32^{+0.37}_{-0.41}$	$0.77^{+0.07}_{-0.08}$	$1.11^{+0.10}_{-0.12}$	$12.58^{+0.20}_{-0.33}$
Low L_X RASS-AGN sample	$3.32^{+0.64}_{-0.83}$	$1.73^{+0.40}_{-0.27}$	$3.26^{+0.58}_{-0.69}$	$0.62^{+0.10}_{-0.12}$	$0.88^{+0.14}_{-0.17}$	$11.83^{+0.55}_{-\infty}$
High L_X RASS-AGN sample	$5.44^{+0.71}_{-0.98}$	$1.86^{+0.20}_{-0.21}$	$5.52^{+0.64}_{-0.71}$	$0.98^{+0.15}_{-0.18}$	$1.44^{+0.22}_{-0.27}$	$13.10^{+0.24}_{-0.43}$

NOTE. — Values are obtained from a fit to $w_p(r_p)$ in a range of $0.3\text{--}15 h^{-1}$ Mpc for all samples using the full error covariance matrix.

$\sigma_8(z=0) = 0.8$ which is consistent with the *Wilkinson Microwave Anisotropy Probe (WMAP)* DR5 for a $\Lambda\text{CDM}+\text{SZ}+\text{LENS}$ model⁶. The errors on b are derived from the standard deviation of $\sigma_{8, \text{AGN}}$.

Because we measure the CCF to infer the ACF, the resulting effective redshift distribution for the clustering signal is determined by both the redshift distribution of the LRG sample and the RASS-AGN sample: $N_{\text{CCF}}(z) = N_{\text{LRG}}(z) * N_{\text{RASS-AGN}}(z)$. The median redshift of $N_{\text{CCF}}(z)$ is $\bar{z}_{\text{CCF}} = 0.27, 0.24, 0.31$ for the total, the low L_X , and the high L_X RASS-AGN samples, respectively. The difference compared to the mean redshift of the different RASS-AGN samples (see Table 1) is at most $\Delta z = 0.03$. Our measurements of $\sigma_{8, \text{AGN}}$ and $b(z)$ (using \bar{z}_{CCF}) for all RASS-AGN samples are listed in Table 3.

If RASS-AGNs are hosted by typical L^* galaxies, the fraction of L^* galaxies hosting RASS-AGNs can be calculated using the observed number density of both host galaxies and RASS-AGNs. Blanton et al. (2003b) measure the number density of L^* galaxies at $z = 0.1$ to be $\phi_{r\text{-band}}^* = 0.0149 \pm 0.0004 h^3 \text{ Mpc}^{-3}$. Using the observed number density in the total RASS-AGN sample (Table 1), we find that only $\sim 0.4\%$ of L^* galaxies could harbor RASS-AGNs.

3.4. Host Dark Matter Halo Mass

Our clustering results can be used to estimate the “typical” dark matter halo mass M_{DMH} hosting our different AGN samples. The dark matter halo mass is reflected by the bias parameter b , which reflects the clustering amplitude relative to the underlying dark matter distribution. Using Equation 8 of Sheth et al. (2001), we com-

⁶ http://lambda.gsfc.nasa.gov/product/map/dr3/params/lcdm_sz_lensmap5.htm

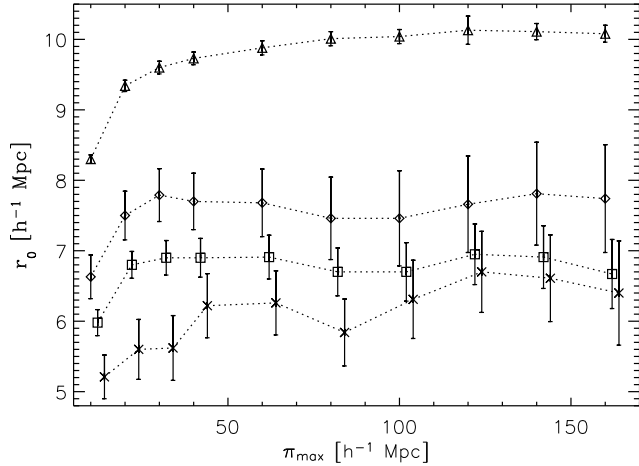


FIG. 5.— Correlation length r_0 vs. π_{\max} using Equation (5) for the LRG ACF (triangles), the high L_X RASS-AGN-LRG CCF (diamonds), the total RASS-AGN-LRG CCF (boxes; for illustration purposes, this has been shifted +2.0 in π_{\max} direction), the low L_X RASS-AGN-LRG CCF (crosses; shifted by +4.0 in π_{\max} direction).

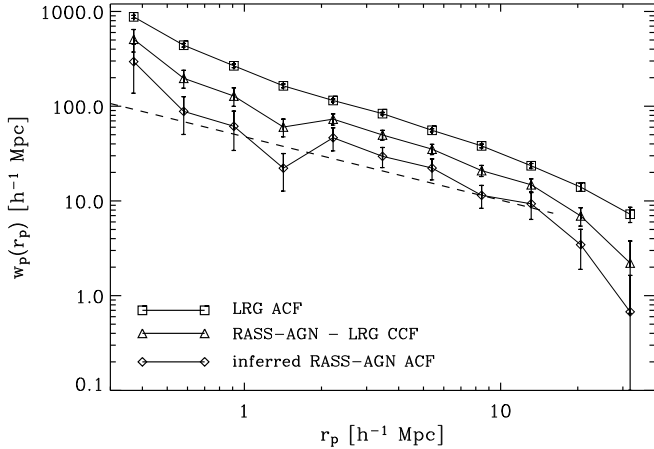


FIG. 6.— Projected LRG ACF (boxes), RASS-AGN-LRG CCF (triangles), and the inferred RASS-AGN ACF (diamonds). For all data points, we show the 1σ uncertainties. The obtained best power law fit of the RASS-AGN ACF, using the covariance matrix and fitting over $r_p = 0.3 - 15 h^{-1}$ Mpc, is shown as a dashed line.

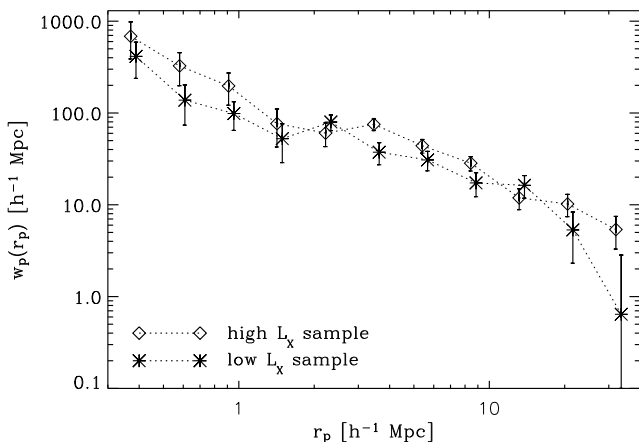


FIG. 7.— CCFs of the low (stars) and high (diamonds) L_X RASS-AGN samples are shown with their corresponding uncertainties.

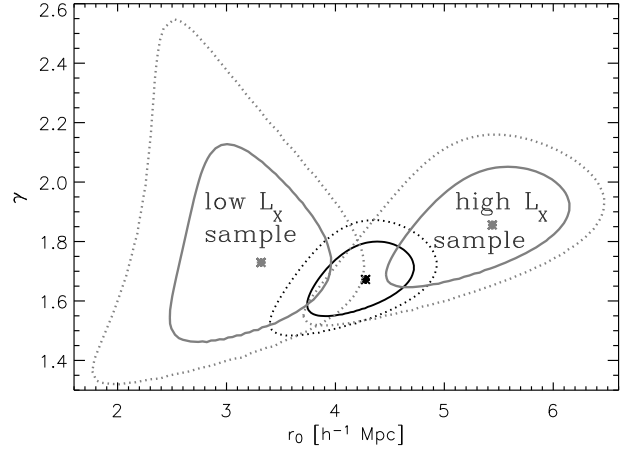


FIG. 8.— Probability contours for the power law normalization r_0 and slope γ of the total RASS-AGN sample (black, central contour), low L_X RASS-AGN sample (gray, left contour), and high L_X RASS-AGN sample (gray, right contour). The solid contours represent the 1σ confidence intervals (68.3%) for a one-parameter fit based on a correlated $\chi^2 = \chi^2_{\min} + 1.0$ (Equation (12)), while the dotted lines illustrate the corresponding intervals for a two-parameter fit (1σ , correlated $\chi^2 = \chi^2_{\min} + 2.3$).

pute the expected large-scale Eulerian bias factor for different dark matter halo masses. The required ratio of the critical overdensity to the rms fluctuation on a given size and mass is calculated by $\nu = \delta_{\text{cr}}/\sigma(M, z)$ (Sheth et al. 2001). Assuming $\delta_{\text{cr}} \approx 1.69$, we compute $\sigma(M, z)$ using Equations (A8), (A9), and (A10) from van den Bosch (2002); this approach was also used in Hickox et al. (2009). The typical dark matter halo mass for the total RASS-AGN and the high L_X RASS-AGN sample is found to be $\log(M_{\text{DMH}}/(h^{-1} M_{\odot})) = 12.58^{+0.20}_{-0.33}$, $13.10^{+0.24}_{-0.43}$, respectively. For the low L_X RASS-AGN sample ($\log(M_{\text{DMH}}/(h^{-1} M_{\odot})) = 11.83^{+0.55}$) we are not able to constrain a lower limit on the dark matter halo mass. This is because our lower limit corresponds to $b = 0.71$ and the minimum b value derived from Sheth et al. (2001) at $z = 0.24$ is $b_{\min} = 0.72$ (at $M_{\text{DMH}} \sim 10^{9.3} h^{-1} M_{\odot}$).

4. DISCUSSION

4.1. Comparison to Other X-ray Clustering Measurements

Our findings can be directly compared to previous attempts to measure the spatial ACF (using spectroscopic redshifts) of low- z RASS-based AGNs at similar X-ray luminosities. Grazian et al. (2004) found a redshift-space clustering length of $s_0 = 8.64^{+2.00}_{-2.08} h^{-1}$ Mpc in the ASIAGO-ESO/RASS QSO survey when fitting their correlation function with γ fixed at 1.56. They did not publish results for fits of r_0 and γ . A second low- z RASS-AGN clustering study with very similar AGN properties was conducted by Mullis et al. (2004) in the *ROSAT* North Ecliptic Pole survey. Their best-fit values are $r_0 = 7.5^{+2.7}_{-4.2} h^{-1}$ Mpc and $\gamma = 1.85^{+1.90}_{-0.80}$. Our inferred ACF of the total RASS-AGN sample yield $r_0 = 4.28^{+0.44}_{-0.54} h^{-1}$ Mpc and $\gamma = 1.67^{+0.13}_{-0.12}$. Both studies used Poisson errors which underestimate systematic effects. Using the largest sample of X-ray selected AGNs ever applied to clustering measurements, and by measuring the cross-correlation with more numerous galaxies, we reach

significantly lower uncertainties compared to the previous studies and detect a clustering signal at the $\sim 11\sigma$ level. We also find a much smaller correlation length. Grazian et al. (2004) and Mullis et al. (2004) derive their results from fitting the ACF at much larger separations (s , r_P values) than we do. However, considering their larger uncertainties, their correlation lengths differ from ours by only 1σ – 2σ . The low number of X-ray selected AGNs used in both studies did not allow them to split their samples in bins of either luminosity or redshift.

At higher redshift, data from more modern X-ray telescopes such as *XMM-Newton* and *Chandra* have been used to measure the clustering of X-ray selected AGNs in various deep survey fields (Table 4). These surveys are significantly more sensitive than *ROSAT* surveys but have sampled smaller comoving volumes (due to smaller sky area coverage) and may therefore be affected by cosmic variance. The median X-ray luminosity of these surveys is roughly 1 mag fainter than the X-ray luminosities detected in *ROSAT*-based catalogs. Furthermore, *XMM-Newton* and *Chandra* are sensitive at both soft energy bands (as *ROSAT*: 0.1–2.4 keV) and hard energy bands (2–10 keV). This influences the sample selection; *ROSAT* samples are dominated by X-ray unabsorbed type I AGNs, while *XMM-Newton* and *Chandra* samples consist of a nearly equal mix of type I AGNs and absorbed type II AGNs. A direct comparison of *ROSAT* and *XMM-Newton/Chandra* AGN clustering measurements is therefore challenging.

The inferred typical host dark matter mass for RASS-AGNs at $z = 0.27$ is consistent with that found at higher redshift in CDFN and AEGIS, though other X-ray AGN clustering studies find significant larger values at these redshifts (i.e., CDFS, CLASXS, and COSMOS; see Table 4 for details).

One possible explanation of the differences in the clustering signals between the low and high- z results could be the presence of a large fraction of type II AGNs in the *XMM-Newton* and *Chandra* samples. However, Gilli et al. (2005, 2009) measured the correlation strengths separately for soft and hard AGN samples, as well as for broad emission line versus narrow emission line AGN samples, and did not find a significant difference. However, larger samples with smaller uncertainties are needed to definitively test this question. Gilli et al. (2005, 2009) explain the large values of r_0 in the CDFS and COSMOS by the cosmic variance, i.e., very prominent redshift spikes at $z \sim 0.7$ and $z \sim 0.36$, respectively. Removing these overdensities in the total X-ray sample results in correlation lengths of $r_0 = 3.8^{+1.3}_{-2.7}$, 6.1 ± 0.8 h^{-1} Mpc, respectively, similar to the values found here at lower redshift. This result underscores the need to include cosmic variance errors when using samples that do not probe a large volume. Among measurements that correctly account for cosmic variance, cosmic evolution and differences in X-ray luminosity may be responsible for the different clustering results in the literature. We will discuss this point in detail in Section 4.3.

In Table 4, we compare the main properties of the different clustering measurements of AGNs selected at different wavelengths (e.g., X-ray and optical) and star-forming and quiescent (i.e., blue and red) galaxies at similar redshifts. Table 4 aims to compare different stud-

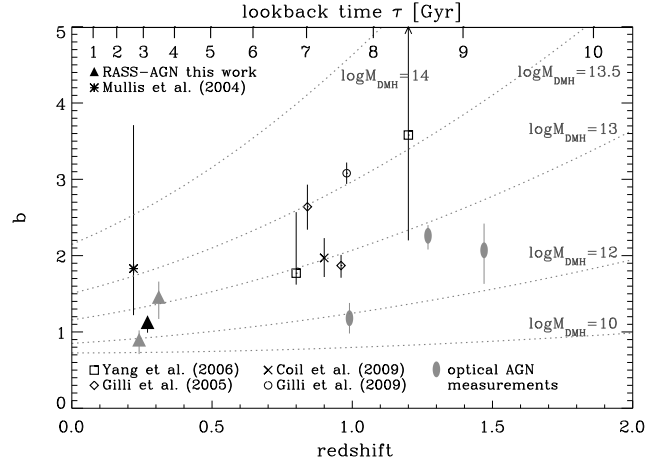


FIG. 9.— Bias parameter $b_{\text{AGN}} = \sigma_{8,\text{AGN}}(z)/[\sigma_8 D(z)]$ as a function of redshift for various X-ray AGN selected samples (see the text for details). Gray triangles represent luminosity-dependent subsamples of the main AGN sample used here. The gray filled ellipses indicate optical AGN clustering measurements (left to right: Coil et al. (2007); Ross et al. (2009); Porciani et al. (2004)). The dotted lines show the expected $b(z)$ of typical dark matter halo masses M_{DMH} based on Sheth et al. (2001). The masses are given in $\log M_{\text{DMH}}$ in units of $h^{-1} M_{\odot}$.

ies as uniformly as possible to detect general trends in the clustering of AGNs to $z \sim 1$. Therefore only studies that are based on the real-space correlation function $\xi(r)$ are included here. Many results, especially for optically selected AGNs, measure only the redshift-space correlation function, $\xi(s)$, and attempt to model redshift-space distortions to infer $\xi(r)$. However, $\xi(s)$ is not well-approximated by a power law and the derived results depend therefore on the fitted s range. Additionally, systematic uncertainties in the modeling make direct comparisons to $\xi(r)$ measurements extremely difficult. To facilitate comparison between samples, we recalculate the bias, $b(z)$, for each study given in Table 4 in a consistent manner. Values of $\sigma_{8,\text{AGN}/\text{GAL}}$ are computed using confidence contours in r_0 – γ space (where $\chi^2 = \chi_{\text{bestfit}}^2 + 1$) published in the literature. If no confidence contours are given, we use the best-fit r_0 , γ values and propagate their error to derive the 1σ error on $\sigma_{8,\text{AGN}/\text{GAL}}$. We exclude papers that report only b values but do not publish r_0 and γ values. Where possible, we report the median redshift of objects in each study that contribute to the clustering signal. We use z_{eff} whenever available, otherwise we use the median redshift (\bar{z}), or the mean redshift ($\langle z \rangle$), in that order, to compute $\sigma_8(z)$ using our normalization of $\sigma_8(z=0) = 0.8$ throughout.

Figure 9 shows the derived bias factors b of various X-ray selected AGN samples as a function of redshift. The results shown in this figure suggest that high redshift, low X-ray luminous AGNs tend to reside in higher mass dark matter halos ($M_{\text{DMH}} \sim 10^{13} h^{-1} M_{\odot}$) than low redshift, high luminous AGNs. Broad-line X-ray and optical AGN measurements seem to show a lower bias values than the narrow-line and/or fainter X-ray AGN measurements.

4.2. Comparison to AGN Clustering Measurements at Different Wavelengths

TABLE 4. COMPARISON OF PUBLISHED REAL-SPACE CLUSTERING MEASUREMENTS OF X-RAY SELECTED AGNS AND OPTICALLY SELECTED AGNS, AS WELL AS RED AND BLUE GALAXIES.

Sample	r_0 (h^{-1} Mpc)	γ	Fitted Range	Area (deg ²)	Object Number	L, M (erg/s), (mag)	Band (keV), filter	z	Bias b	Ref.
RASS	$4.28^{+0.44}_{-0.54}$	$1.67^{+0.13}_{-0.12}$	0.3-15	5468	1552	1.4×10^{44}	0.1-2.4	0.27	$1.11^{+0.10}_{-0.12}$	This work
Low- L RASS	$3.32^{+0.64}_{-0.83}$	$1.73^{+0.40}_{-0.27}$	0.3-15	5468	990	9.8×10^{43}	0.1-2.4	0.24	$0.88^{+0.14}_{-0.17}$	This work
High- L RASS	$5.44^{+0.71}_{-0.98}$	$1.86^{+0.20}_{-0.21}$	0.3-15	5468	562	3.4×10^{44}	0.1-2.4	0.31	$1.44^{+0.22}_{-0.27}$	This work
X-ray Selected AGN Clustering Measurements										
NEP	$7.5^{+2.7}_{-4.2}$	$1.85^{+1.90}_{-0.80}$	5-60 ^P	80.7	219	9.2×10^{43}	0.5-2.0	0.22 ^E	$1.83^{+1.88}_{-0.61}$	Mu04
CDFN	5.5 ± 0.6	1.50 ± 0.12	0.2-10 ^P	0.13	160	1×10^{43}	0.5-10	0.96	$1.87^{+0.14}_{-0.16}$	Gi05
CDFS	10.3 ± 1.7	1.33 ± 0.14	0.2-10 ^P	0.1	97	1.6×10^{43}	0.5-10	0.84	$2.64^{+0.29}_{-0.30}$	Gi05
CLASSXS	$8.1^{+1.2}_{-2.2}$	2.1 ± 0.5	1-30	0.4	233	9×10^{43}	2-8	1.2	$3.58^{+2.49}_{-1.38}$	Ya06
CDFN	$5.8^{+1.0}_{-1.5}$	$1.38^{+0.12}_{-0.14}$	0.2-15	0.13	252	3×10^{42}	2-8	0.8	$1.77^{+0.80}_{-0.15}$	Ya06
AEGIS	5.95 ± 0.90	1.66 ± 0.22	0.1-8	0.63	113	6.3×10^{42}	2-10	0.90	$1.97^{+0.26}_{-0.25}$	Co09
COSMOS	$8.65^{+0.41}_{-0.48}$	$1.88^{+0.06}_{-0.07}$	0.3-40 ^P	1.96	538	6.3×10^{43}	0.5-10	0.98	$3.08^{+0.14}_{-0.14}$	Gi09
Optically Selected AGN Clustering Measurements										
2QZ	$4.8^{+0.9}_{-1.5}$	$1.53^{+0.19}_{-0.21}$	0.8-20	~ 700	13989	-23.82	b_J	1.47 ^E	$2.07^{+0.35}_{-0.44}$	Po04
2QZ-sub1	$5.4^{+0.9}_{-1.3}$	$2.02^{+0.36}_{-0.33}$	2-20	~ 700	4928	-23.13	b_J	1.06 ^E	$2.14^{+0.71}_{-0.55}$	Po04
2QZ-sub2	$4.3^{+1.8}_{-2.0}$	$1.49^{+0.32}_{-0.35}$	2-20	~ 700	4737	-23.84	b_J	1.51 ^E	$1.93^{+0.73}_{-0.90}$	Po04
2QZ-sub3	$7.6^{+1.2}_{-2.1}$	$1.79^{+0.25}_{-0.29}$	2-20	~ 700	4324	-24.30	b_J	1.89 ^E	$3.71^{+0.97}_{-1.03}$	Po04
DEEP2	3.1 ± 0.6	1.8(fixed)	0.1-10	3	52	-23.0	B	0.99	$1.18^{+0.20}_{-0.20}$	Co07
SDSS	$5.45^{+0.35}_{-0.45}$	$1.90^{+0.04}_{-0.03}$	1-130	~ 4000	30239	~ -25.8	i	$\langle 1.27 \rangle$	$2.26^{+0.14}_{-0.18}$	Ro09
Galaxy Clustering Measurements										
red-2dF	6.10 ± 0.34	1.95 ± 0.03	0.2-20	~ 700	36318	1.26	L^*	0.11	$1.41^{+0.08}_{-0.08}$	Ma03
blue-2dF	3.67 ± 0.30	1.60 ± 0.04	0.2-20	~ 700	60473	0.95	L^*	0.11	$0.85^{+0.05}_{-0.05}$	Ma03
red-SDSS	5.67 ± 0.37	2.08 ± 0.05	0.1-10	2497	5804	$\langle -19.5 \rangle$	r	$\langle 0.05 \rangle$	$1.41^{+0.09}_{-0.09}$	Ze05b
blue-SDSS	3.63 ± 0.16	1.69 ± 0.04	0.1-10	2497	8419	$\langle -19.5 \rangle$	r	$\langle 0.05 \rangle$	$0.86^{+0.03}_{-0.04}$	Ze05b
LRG-SDSS	9.80 ± 0.20	1.94 ± 0.02	0.3-30	~ 3800	29298	$\langle -21.63 \rangle$	$gz=0.3$	$\langle 0.28 \rangle$	$2.56^{+0.06}_{-0.06}$	Ze05a
red-AGES	5.3 ± 0.2	2.1 ± 0.1	0.3-10	7	3146	-21.3	$r_{z=0.1}$	0.41	$1.59^{+0.06}_{-0.06}$	Hi09
blue-AGES	3.8 ± 0.2	1.6 ± 0.1	0.3-10	7	3116	-21.0	$r_{z=0.1}$	0.38	$1.07^{+0.05}_{-0.05}$	Hi09
red-DEEP2	5.25 ± 0.26	2.06 ± 0.04	0.1-20	3	1474	-20.70	B	$\langle 0.82 \rangle$	$1.88^{+0.09}_{-0.09}$	Co08
blue-DEEP2	3.87 ± 0.12	1.64 ± 0.05	0.1-20	3	4808	-20.48	B	$\langle 0.90 \rangle$	$1.39^{+0.04}_{-0.04}$	Co08
red-VVDS	$3.78^{+0.70}_{-0.74}$	$1.87^{+0.28}_{-0.22}$	0.1-10	0.5	355	-19.57	B_{AB}	0.81 ^E	$1.31^{+0.23}_{-0.24}$	Me06
blue-VVDS	$2.49^{+0.28}_{-0.22}$	$1.84^{+0.14}_{-0.10}$	0.1-10	0.5	1105	-19.75	B_{AB}	1.04 ^E	$0.98^{+0.10}_{-0.08}$	Me06

NOTE. — Values for the fitted range (Column 4) are in units of h^{-1} Mpc. Values listed for L and M are the median values whenever these quantities were available. Otherwise, mean values are given and denoted by angled brackets ($\langle \rangle$). Superscript “P” on the fitted range indicates that only Poisson errors have been used for the fit, which causes a significant underestimation of the uncertainties. All other studies used either the bootstrap or jackknife method to estimate their uncertainties. Superscript “E” shows that the effective redshift was given in the study, as opposed to the median redshift. Abbreviation: subs—subsample. References: Gr04—Grazian et al. (2004); Mu04—Mullis et al. (2004); Gi05—Gilli et al. (2005); Ya06—Yang et al. (2006); Co09—Coil et al. (2009); Gi09—Gilli et al. (2009); Hi09—Hickox et al. (2009); Po04—Porciani et al. (2004); Co07—Coil et al. (2007); Ro09—Ross et al. (2009); Ma03—Madgwick et al. (2003); Ze05b—Zehavi et al. (2005b) Ze05a—Zehavi et al. (2005a); Co08—Coil et al. (2008); Me06—Meneux et al. (2006).

The availability of large optical data sets such as SDSS, 2dF QSO Redshift Survey (2QZ), and 2dF-SDSS LRG and QSO (2SLAQ) led to a series of large-scale clustering studies. However, many authors report only $\xi(s)$ (e.g., Croom et al. 2005; da Ângela et al. 2008), which makes it difficult to compare their results to our $\xi(r)$ -based results. Other studies compute the CCF between optically selected QSOs and LRGs (e.g., Mountrichas et al. 2009), but do not infer the QSO ACF. Here we compare only to studies that measured $\xi(r)$, listed in Table 4 (middle section). Most of the optically selected AGN samples contain samples that are orders of magnitude larger than X-ray selected samples. Coil et al. (2007) use the CCF between ~ 5000 DEEP2 galaxies and 52 QSOs to infer the QSO ACF.

AGNs selected at optical wavelengths have relatively low clustering scale lengths, found over a wide range of redshifts. This translates into low bias parameters, not much larger than what we find for our low- z RASS-AGNs (Figure 10). Radio-loud AGNs are found to be significantly more clustered than optically selected AGNs (e.g., Magliocchetti et al. 2004; Hickox et al. 2009; Mandelbaum et al. 2009). Optically bright and radio-loud quasars are also luminous in X-rays (Wilkes et al. 1994) and reside in very massive dark matter halos (e.g., Shen et al. 2009).

Comparing the general trends seen in Figure 9 and 10, X-ray and optically selected AGNs show similar clustering strength at $z < 1$. Optically selected AGNs at higher redshifts are found to have a lower clustering

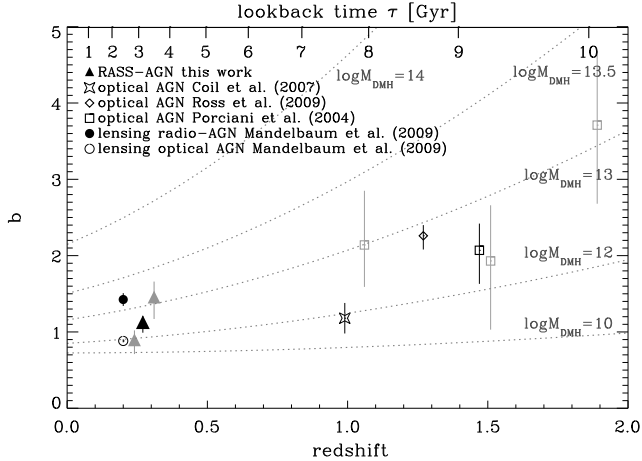


FIG. 10.— Similar to Figure 9, now comparing our results to AGN samples selected at optical and radio wavelengths. Our results are shown at $z = 0.3$; gray triangles represent subsamples of the main AGN sample used here; gray boxes show subsamples of the AGN sample by Porciani et al. (2004).

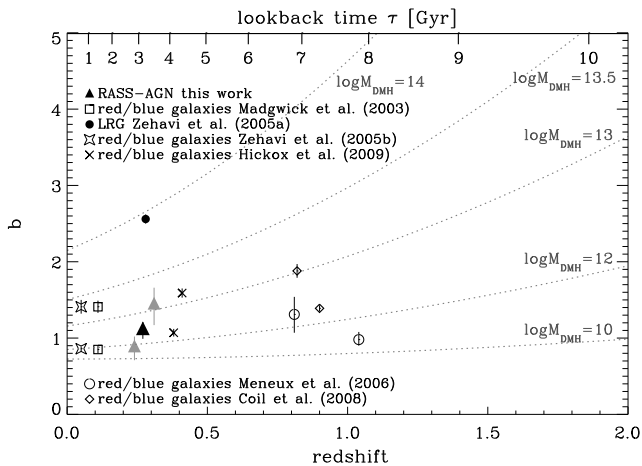


FIG. 11.— Similar to Figure 9, now comparing our results to red and blue galaxy samples. For all galaxy results, the data point with lower b value corresponds to blue, star-forming galaxies while red galaxies have higher b values.

than X-ray selected AGNs. The sample of Porciani et al. (2004) has a higher mean luminosity and higher clustering signal than the sample of Coil et al. (2007). Within the errors, the clustering of optically selected AGNs is known to be in accordance with a redshift-independent dark matter halo mass of $M_{\text{DMH}} \sim 10^{12} - 10^{13} h^{-1} M_{\odot}$ (Porciani et al. 2004; Coil et al. 2007; Ross et al. 2009). Low-luminosity AGNs ($-23 < M_{0.1r} < -17$) in the local universe have a typical dark matter halo mass of $M_{\text{DMH}} \sim 8 \times 10^{11} h^{-1} M_{\odot}$ (Mandelbaum et al. 2009), which is also consistent with the M_{DMH} given by Porciani et al. (2004) and Coil et al. 2007 for the high-redshift luminous AGNs considering the uncertainties in their clustering measurements.

4.3. Luminosity Dependence of the Clustering Signal

In the hierarchical model of structure formation, more massive galaxies should reside in more massive dark matter halos and therefore be more strongly clustered. More massive galaxies are expected to be more lumi-

nous, which should lead to a luminosity dependence of the clustering signal. This result has been confirmed by clustering measurements of, e.g., SDSS galaxies at low redshifts (Zehavi et al. 2005b) and of, e.g., DEEP2 galaxies at $z = 1$ (Coil et al. 2006). Whether this relation applies also to the AGN luminosity is unclear. The AGN luminosity depends on the SMBH mass, mass accretion rate, and radiative accretion efficiency. In the simple case in which all SMBHs have the same Eddington ratio and the same dependence of radiative efficiency on the Eddington ratio, then higher-luminosity AGNs will have higher SMBH masses. *If* there is a correlation between SMBH mass and dark matter halo mass, then the higher-luminosity AGNs will also be more strongly clustered. The observed correlation between the mass of the SMBH and the stellar velocity dispersion in the bulge of the galaxy (Gebhardt et al. 2000; Ferrarese & Merritt 2000) suggests that a luminosity (X-ray and optical) clustering dependence could be feasible and physically motivated, since massive bulges preferentially reside in massive DMHs. Alternatively, even among galaxies with the same SMBH mass, those that reside in a denser large-scale environment may have a higher chance of large mass accretion through galaxy mergers and interactions. However, this trend has not been detected, possibly due in part to the relatively large uncertainties in the clustering measurements of X-ray and optically selected AGN samples.

Several studies have attempted to measure the dependence of clustering on X-ray luminosity. Gilli et al. (2009) compute the clustering signal for a high and low X-ray luminosity AGN sample in the *XMM-Newton*-COSMOS field at a dividing line of $L_X^{0.5-10 \text{ keV}} = 10^{44} \text{ erg s}^{-1}$ and find no significant difference. Yang et al. (2006) studied an X-ray luminosity dependence in the *Chandra* selected AGN samples. As noted by both Yang et al. (2006) and Gilli et al. (2009), splitting the samples in different X-ray luminosities leads to the study of a high and low redshift sample of X-ray selected AGNs. These studies of the dependence of clustering on luminosity are therefore hampered by the redshift-luminosity degeneracy. Taking into account the possible redshift evolution of the clustering signal, Yang et al. (2006) do not find a significant dependence of clustering on the X-ray luminosity. Coil et al. (2009) measure the clustering of AGNs with $10^{42} \text{ erg s}^{-1} < L_X^{2-10 \text{ keV}} < 10^{43} \text{ erg s}^{-1}$ and $L_X^{2-10 \text{ keV}} < 10^{42} \text{ erg s}^{-1}$ at similar redshift ($z = 0.8$) and find no significant difference in their clustering properties as well.

Our sample here covers a limited redshift range, $0.16 < z < 0.36$, such that we do not expect a significant contribution of the redshift evolution to the clustering signal within our sample. In addition, our use of the CCF with a large tracer set of LRGs yields an AGN ACF with high precision. Splitting the sample into a low and high X-ray luminosity sample at the commonly used AGN/QSO dividing line of $L_X^{0.5-10 \text{ keV}} = 10^{44} \text{ erg s}^{-1}$ allows us to detect an X-ray luminosity dependence of the clustering at the $\sim 2.5\sigma$ level for the first time, in that X-ray luminous RASS-AGNs at low- z cluster more strongly than their low luminosity counterparts.

Although, as mentioned above, the tracer LRG sample is approximately volume-limited, in order to clearly test

whether the difference in the clustering signal between the high and the low L_X RASS-AGN sample could be caused by a change of the LRG ACF with redshift (which could mimic a luminosity dependence of the inferred RASS-AGN ACF), the redshift dependence of the LRG sample ACF must be analyzed. Zehavi et al. (2005a) study dependence of the LRG clustering amplitude with luminosity and redshift and split their $0.16 < z < 0.36$ LRG sample into $0.16 < z < 0.23$ and $0.23 < z < 0.36$ subsamples; they find no redshift evolution in the LRG clustering signal. We repeat this test and split our LRG sample into two subsamples containing object in redshift bins of $0.16 < z < 0.26$ and $0.26 < z < 0.36$. We verify that the LRG ACF of both subsamples agree to much better than 1σ and therefore exclude redshift evolution of the LRG clustering signal as a possible source of the detected luminosity dependence of the RASS-AGN clustering.

Optical QSO/AGN samples based on SDSS, 2QZ, and 2SLAQ samples yield comparable low uncertainties in the measured ACF due to the large sample sizes (up to a few 10,000 objects), allowing measurements of the luminosity dependence of clustering in optically selected QSO/AGN samples. Mountrichas et al. (2009) compute the CCF at $z < 1$ between QSOs and LRGs from 2SLAQ, 2QZ, and SDSS to break the redshift-luminosity degeneracy. They find little QSO-LRG cross-clustering dependence on QSO luminosity, implying dark matter halo masses of $M_{\text{DMH}} \sim 10^{13} h^{-1} M_{\odot}$ approximately independent of QSO luminosity. Da Ângela et al. (2008) confirm that QSOs of different luminosities reside in dark matter halos of similar mass ($M_{\text{DMH}} \sim 3 \times 10^{12} h^{-1} M_{\odot}$) for $z \sim 1.5$.

Using the optical luminosity in Table 4 and the α_{ox} relation between the optical rest-frame flux density at 2500 Å and the X-ray luminosity flux density at 2 keV measured for 6224 AGNs with broad emission lines from Anderson et al. (2007), we derive the median X-ray luminosities of the optical AGN samples. This allows us to compare these results with X-ray selected AGN clustering measurements. The optically selected AGN samples have median X-ray luminosities of $L_X^{0.1-2.4 \text{ keV}} \sim 3 - 9 \times 10^{44} \text{ erg s}^{-1}$, which is very similar to the X-ray luminosity of our high L_X RASS-AGN sample. These samples are shown in Figure 9 as gray filled ellipses. Contrary to our findings for the X-ray luminosity dependence at low- z , at higher redshift high luminosity optically selected AGNs appear to be *less* clustered than low luminosity X-ray selected AGNs. This implies that high luminosity AGNs at these redshifts lie in less massive dark matter halos than low luminosity AGNs. However, *Chandra* and *XMM-Newton* X-ray selected AGNs (which define the X-ray samples at higher redshift) contain a significant fraction of type II AGNs, while optically selected AGN samples contain mainly type I AGNs with broad optical emission lines. Therefore, X-ray and optically selected samples at high redshifts probe different kinds of AGNs. Optically selected, high luminosity AGN samples at high redshifts and high L_X RASS-AGN samples at low redshifts likely contain the same type of AGNs because of both *ROSAT*'s soft energy selection being biased toward X-ray unabsorbed type I AGNs and the similar X-ray luminosities measured for both samples. In terms of their clustering properties, optically selected AGN samples at

higher redshift reside in host dark matter halo masses between $M_{\text{DMH}} \sim 10^{12} h^{-1} M_{\odot}$ and $M_{\text{DMH}} \sim 10^{13} h^{-1} M_{\odot}$, similar to the full range observed for the low redshift RASS-AGN samples. Stated differently, the dark matter halo masses of both the low L_X and high L_X RASS-AGN samples are consistent with those of the optically selected, high luminosity AGNs at higher redshift (which have relatively large clustering uncertainties).

To summarize the clustering trends seen, at low redshift within the RASS-AGN broad-line sample, higher luminosity AGNs cluster more strongly than their lower luminosity counterparts, while at higher redshifts ($z \gtrsim 0.7$) the higher luminosity optically selected AGNs are less clustered than the lower luminosity X-ray selected AGNs. However, the higher redshift X-ray AGN samples contain a large fraction of narrow-line AGNs, and so these trends are not necessarily comparing the same kinds of AGNs at all redshifts and luminosities. For example, the low L_X AGNs studied at high redshifts have lower luminosities than the low redshift, low L_X RASS-AGNs (see Table 4). We propose two possible explanations for the AGN clustering trends observed, assuming the validity of the α_{ox} connection, i.e., that over a wide range of X-ray and optical luminosity, both luminosities are closely connected independent of redshift:

1) The dominant accretion processes that are triggering AGN activity could be different at different redshifts and/or halo masses. For example, one possible scenario is that at high redshift AGNs may be triggered by interactions or mergers between galaxies in group environments, while at low redshifts internal processes might be responsible. Consequently, due to different underlying physics triggering AGN activity, the observed AGN clustering properties at low and high redshifts could differ.

2) Alternatively, the underlying physics may not evolve with time, but the kinds of AGNs being compared at different redshifts and luminosities are fundamentally different. It may be that high luminosity broad-line AGNs generally reside in lower mass dark matter halos (at least out to $z \sim 1$), and within this population the brighter AGNs are more clustered. On the other hand, the lower luminosity AGNs probed in the deep $z \sim 1$ surveys, which contain a mix of broad-line and narrow-line AGNs, may reside in more massive halos. In this scenario, different kinds of AGNs can have different triggering mechanisms. The change in the luminosity dependence of the clustering signal seen with cosmic time is simply explained by observing different kinds of AGNs in the low and high redshift universe with current data sets.

The present clustering measurements do not allow us to accept or reject these hypotheses; smaller uncertainties on the observed clustering and detailed model predictions are needed. However, it is clear from the above results and discussion that there is not a simple relation between luminosity and clustering amplitude for AGNs.

4.4. Comparison to Galaxy Clustering

Large-scale structure studies have established the dependence of galaxy clustering on morphological type, luminosity, color, spectral type, and stellar mass (e.g., Norberg et al. 2002; Madgwick et al. 2003; Zehavi et al. 2005b; Meneux et al. 2006, 2009; Coil et al. 2008). These quantities are strongly correlated with each other and with clustering amplitude. For a comparison with

our AGN clustering measurements, we focus on the color-dependence of galaxy clustering. The last section of Table 4 lists a representative sample of the color-dependent clustering measurements of galaxies to $z = 1$, where we have listed results for galaxies with $L \sim L^*$, where we use Blanton et al. (2003b); Norberg et al. (2002), and Willmer et al. (2006) to determine L^* for each sample. The Meneux et al. (2006) results in Table 4 correspond to galaxies 1 mag below M^* but contain more objects and therefore yield more reliable clustering measurements.

Blue galaxies show a weaker clustering signal than red galaxies over the wide redshift range studied here ($0.07 < z < 1.0$). At low redshifts, results from larger surveys agree with each other and indicate that red galaxies are hosted by dark matter halos of slightly higher mass than $M_{\text{DMH}} \sim 10^{13} h^{-1} M_{\odot}$, while blue galaxies reside in halos of $M_{\text{DMH}} \sim 10^{12} h^{-1} M_{\odot}$. At $z > 0.5$ different studies find that red galaxies are more strongly clustered than blue galaxies, but the published clustering scale lengths are discrepant. In terms of inferred dark matter halo masses, our measurements are in agreement with Coil et al. (2007), while the results by Meneux et al. (2006) give dark matter halo masses which are too low when evolve into low- z L^* galaxies. The errors on the measurements of optical AGN clustering are too large to constrain the host galaxy type using the clustering measurements; the results are consistent with optical AGNs being hosted by either blue or red galaxies. However, Coil et al. (2007) find that at the 2σ level QSOs are clustered like blue galaxies, not red, at $z = 1$.

Our clustering measurements strongly exclude the possibility that RASS-AGNs reside in the very massive dark matter halos that host LRGs (Figure 11). Interestingly, our sample of ~ 1000 low L_X RASS-AGNs clusters similarly to blue galaxies, while the high L_X RASS-AGNs ($n = 562$) have the same clustering amplitude as red galaxies at similar redshifts. This suggests that RASS-AGNs are hosted in a mix of higher fraction of blue galaxies and lower fraction of red galaxies.

5. CONCLUSIONS

Using cross-correlation measurements between RASS-AGNs and SDSS LRGs, we measure the projected cross-correlation $w_p(r_p)$, and from this we derive the real-space auto-correlation function $\xi(r)$ of X-ray selected AGNs with broad optical emission lines at $\langle z \rangle = 0.25$ with an unprecedented precision. Using the RASS/SDSS cross-identification sample by Anderson et al. (2007) results in the largest sample of X-ray selected AGNs ($n = 1552$) used for clustering studies, covering an area of 5468 deg^2 . We detect a clustering signal at the $\sim 11\sigma$ level and find a correlation length of $r_0 = 4.28_{-0.54}^{+0.44} h^{-1} \text{ Mpc}$ and $\gamma = 1.67_{-0.12}^{+0.13}$, fitting on scales of $r_p = 0.3 - 15 h^{-1} \text{ Mpc}$.

We investigate the luminosity dependence of clustering using low and high X-ray luminosity subsamples defined using the common AGN/QSO dividing line of $L_X^{0.5-10 \text{ keV}} = 10^{44} \text{ erg s}^{-1}$. We detect an X-ray luminosity dependence of the clustering signal at the $\sim 2.5\sigma$ level, with the brighter sample being more clustered. This is contrasted with clustering measurements of low luminosity X-ray AGNs and optically selected QSOs at redshift $z > 0.5$, which suggest that low X-ray luminosity AGNs are more strongly clustered and reside in more massive dark matter halos than their high X-ray luminosity coun-

terparts. Possible explanations are that (1) different mechanisms trigger AGN activities at different redshifts and/or halo masses or (2) at all redshift, low luminosity AGNs and the brightest QSOs reside in red galaxies, while most intermediate luminosity AGNs/QSOs are hosted in blue galaxies.

Our low L_X RASS-AGN sample exhibits a similar clustering amplitude as blue, star-forming galaxies at similar redshifts, while the high L_X RASS-AGN sample clusters like red galaxies. The total RASS-AGN sample is likely dominated by blue host galaxies but includes a fair fraction of red host galaxies.

We show that the auto-correlation function derived from cross-correlation measurements of ~ 1500 AGNs and ~ 50000 LRGs in an area of $\sim 6000 \text{ deg}^2$ constrains the auto-correlation function at the 10% level. Although the RASS is the most sensitive X-ray survey ever performed, only the most luminous and X-ray unabsorbed (soft) AGNs were detected. The upcoming all-sky *eROSITA* mission (Predehl et al. 2007) with its *XMM-Newton*-like soft and hard energy high sensitivity should detect $\sim 200,000$ AGNs with much lower X-ray luminosities. The data generated by the mission will allow one to compute clustering measurements with a significantly higher accuracy.

To draw meaningful conclusions from AGN clustering measurements using AGN samples selected at different wavelengths and to address the evolution and luminosity dependence of AGN clustering, lower uncertainties on the detected clustering signal are required. We describe and successfully show in this paper that the cross-correlation function can be used to not only measure the relative clustering of AGN/galaxy samples but also to determine the auto-correlation function with relatively low uncertainties.

We thank Richard Rothschild, Alex Markowitz, and Slawomir Suchy for helpful discussions. We also like to thank Idit Zehavi for providing the values for the red/blue SDSS galaxy clustering measurements, as well as Ryan C. Hickox for making the median M_B magnitudes for his samples of red and blue galaxies available. Last but not least we thank the anonymous referee for the very detailed and helpful report.

This work has been supported by NASA grant NNX07AT02G, CONACyT Grant Científica Básica No. 83564, and UNAM-DGAPA Grant PAPIIT IN110209.

The *ROSAT* Project was supported by the Bundesministerium für Bildung und Forschung (BMBF/DLR) and the Max-Planck-Gesellschaft (MPG). Funding for the Sloan Digital Sky Survey (SDSS) has been provided by the Alfred P. Sloan Foundation, the Participating Institutions, the National Aeronautics and Space Administration, the National Science Foundation, the U.S. Department of Energy, the Japanese Monbukagakusho, and the Max Planck Society. The SDSS Web site is <http://www.sdss.org/>.

The SDSS is managed by the Astrophysical Research Consortium (ARC) for the Participating Institutions. The Participating Institutions are The University of Chicago, Fermilab, the Institute for Advanced Study, the Japan Participation Group, The Johns Hopkins University, Los Alamos National Laboratory, the

Max-Planck-Institute for Astronomy (MPIA), the Max-Planck-Institute for Astrophysics (MPA), New Mexico State University, University of Pittsburgh, Princeton

University, the United States Naval Observatory, and the University of Washington.

REFERENCES

- Abazajian, K., Adelman-McCarthy, J., Agüeros, M.A., et al. 2004, *AJ*, 128, 502
- Abazajian, K., Zheng, Z., Zehavi, I., et al. 2005, *ApJ*, 625, 613
- Abazajian, K., Adelman-McCarthy, J., Agüeros, M.A., et al. 2009, *ApJS*, 182, 543
- Adelman-McCarthy, J., Agüeros, M.A., Allam, S.S., et al. 2007, *ApJS*, 172, 634
- Akylas, A., Georgantopoulos, I., & Plionis, M. 2000, *MNRAS*, 318, 1036
- Anderson, S.F., Voges, W., Margon, B., et al. 2003, *AJ*, 126, 2209
- Anderson, S.F., Margon, B., Voges, W., et al. 2007, *AJ*, 133, 313
- Avni, Y., & Bahcall, J.N. 1980, *ApJ*, 235, 694
- Becker, R.H., White, R.L., & Helfand, D.J., 1995, *ApJ*, 450, 559
- Blanton, M.R., Lin, H., Lupton, R.H., et al. 2003a, *AJ*, 125, 2276
- Blanton, M.R., Hogg, D.W., Bahcall, N.A., et al. 2003b, *ApJ*, 592, 819
- Blanton, M.R., Schlegel, D.J., Strauss, M.A., et al. 2005, *AJ*, 129, 2562
- Bonoli, S., Marulli, F., & Springel, V. 2009, *MNRAS*, 396, 423
- Cattaneo, A., Dekel, A., Devriendt, J., Guiderdoni, B., & Blaizot, J. 2006, *MNRAS*, 370, 1651
- Coil, A.L., Newman, J.A., Cooper, M.C., et al. 2006, *ApJ*, 644, 671
- Coil, A.L., Hennawi, J.F., Newman, J.A., et al. 2007, *ApJ*, 654, 115
- Coil, A.L., Newman, J.A., Croton, D., et al. 2008, *ApJ*, 672, 153
- Coil, A.L., Georgakakis, A., Newman, J.A., et al. 2009, *ApJ*, 701, 1484
- Colberg, J.M., Di Matteo, T. 2008, *MNRAS*, 387, 1163
- Conroy, C., Gunn, J.E., & White, M. 2009, *ApJ*, 699, 486
- Covey, K.R., Agüeros, M.A., Green, P.J., et al. 2008, *ApJS*, 178, 339
- Croom, S.M., Boyle, B.J., Shanks, T., et al. 2005, *MNRAS*, 356, 415
- da Ángela, J., Shanks, T., Croom, S.M., et al. 2008, *MNRAS*, 383, 565
- Davis, M., Peebles, P.J.E. 1983, *ApJ*, 267, 465
- Di Matteo, T., Springel, V., & Hernquist, L. 2005, *Nature*, 433, 604
- Eisenstein, D.J., Annis, J., Gunn, J.E., et al. 2001, *AJ*, 122, 2267
- Ferrarese, L., Merritt, D. 2000, *ApJ*, 539, 9
- Gebhardt, K., Bender, R., Bower, G., et al. 2000, *ApJ*, 539, 13
- Gilli, R., Daddi, E., Zamorani, G., et al. 2005, *A&A*, 430, 811
- Gilli, R., Zamorani, G., Miyaji, T., et al. 2009, *A&A*, 494, 33
- Grazian, A., Negrello, M., Moscardini, L., et al. 2004, *AJ*, 127, 592
- Hamilton, A.J.S. 2001, *MNRAS*, 322, 419
- Hamilton, A.J.S., Tegmark, M. 2004, *MNRAS*, 349, 115
- Hickox, R.C., Jones, C., Forman, W.R., et al. 2009, *ApJ*, 696, 891
- Kaiser, N. 1987, *MNRAS*, 227, 1
- Kauffmann, G., Haehnelt, M. 2000, *MNRAS*, 311, 576
- Landy, S.D., Szalay, A.S. 1993, *ApJ*, 412, 64
- Li, C., Kauffmann, G., Wang, L., et al. 2006, *MNRAS*, 373, 457
- Madgwick, D.S., Hawkins, E., Lahav, O., et al. 2003, *MNRAS*, 344, 847
- Magliocchetti, M., Maddox, S.J., Hawkins, E., et al. 2004, *MNRAS*, 350, 1485
- Mainieri, V., Bergeron, J., Hasinger, G., et al. 2002, *A&A*, 393, 425
- Mandelbaum, R., Li, C., Kauffmann, G., White, S.D.M., et al. 2009, *MNRAS*, 393, 377
- Meneux, B., Le Fèvre, O., Guzzo, L., et al. 2006, *A&A*, 452, 387
- Meneux, B., Guzzo, L., de la Torre, S., et al. 2009, *A&A*, 505, 463
- Miyaji, T., Zamorani, G., Cappelluti, N., et al. 2007, *ApJS*, 172, 396
- Mountrichas, G., Sawangwit, U., Shanks, T., et al. 2009, *MNRAS*, 394, 2050
- Mullis, C.R., Henry, J.P., Gioia, I.M., et al. 2004, *ApJ*, 617, 192
- Norberg, P., Baugh, C.M., Gaztañaga, E., & Croton, D.J. 2009, *MNRAS*, 396, 19
- Norberg, P., Baugh, C.M., Hawkins, E., et al. 2002, *MNRAS*, 332, 827
- Park, C., Choi, Y., Vogeley, M.S., et al. 2007, *ApJ*, 658, 898
- Peacock, J.A., Cole, S., Norberg, P., et al. 2001, *Nature*, 410, 169
- Peebles, P.J.E., *The Large-Scale Structure of the Universe*, Princeton, N.J., Princeton Univ. Press
- Piconcelli, E., Jimenez-Bailón, E., Guainazzi, M., et al. 2005, *A&A*, 432, 15
- Porciani, C., Magliocchetti, M., Norberg, P. 2004, *MNRAS*, 355, 1010
- Predehl, P., Andritschke, R., Bornemann, W., et al. 2007, *Proc. SPIE*, 6686, 36
- Ross, N.P., Shen, Y., Strauss, M.A., et al. 2009, *ApJ*, 697, 1634
- Savitzky, A., Golay, M.J.E. 1964, *Anal. Chem.*, 36, 1627
- Shen, Y., Strauss, M.A., Ross, N.P., et al. 2009, *ApJ*, 697, 1656
- Sheth, R.K., Mo, H.J., & Tormen, G. 2001, *MNRAS*, 323, 1
- Spergel, D.N., Verde, L., Peiris, H.V., et al. 2003, *ApJS*, 148, 175
- Springel, V., White S.D.M., & Jenkins, A. 2005, *Nature*, 435, 629
- Strauss, M.A., Weinberg, D.H., Lupton, R.H., et al. 2002, *AJ*, 124, 1824
- van den Bosch, F.C. 2002, *MNRAS*, 331, 98
- Voges, W., Aschenbach, B., Boller, T., et al. 1999, *A&A*, 349, 389
- Voges, W., Aschenbach, B., Boller, T., et al. 2000, *IAU Circ.*, 7432, 3
- Wake, D.A., Miller, C.J., Di Matteo, T., et al. 2004, *ApJ*, 610, 85
- Watson, M.G., Schröder, A.C., Fyfe, D., et al. 2009, *A&A*, 493, 339
- Wilkes, B.J., Tananbaum, H., Worrall, D.M., et al. 1994, *ApJS*, 92, 53
- Willmer, C.N.A., Faber, S.M., Koo, D.C., et al. 2006, *ApJ*, 647, 858
- Yang, Y., Mushotzky, R.F., Barger, A.J., & Cowie, L.L. 2006, *ApJ*, 645, 68
- York, D.G., Adelman, J., Anderson, Jr., J.E., et al. 2000, *AJ*, 120, 1579
- Zehavi, I., Blanton, M.R., Frieman, J.A., et al. 2002, *ApJ*, 571, 172
- Zehavi, I., Eisenstein, D.J., Nichol, R.C., et al. 2005a, *ApJ*, 621, 22
- Zehavi, I., Zheng, Z., Weinberg, D.H., et al. 2005b, *ApJ*, 630, 1